Enhancing Room Temperature Performance of Solid-State Lithium Cell via a Facile Solid Electrolyte-Cathode Interface Design

Asish Kumar Das[a], Manish Badole[a], Hari Narayanan Vasavan[a], Samriddhi Saxena[a], Pratiksha Gami[a], Sonia Deswal[b], Pradeep Kumar[b], Sunil Kumar [a,c,*]

[a]Department of Metallurgical Engineering and Materials Science, Indian Institute of Technology Indore, Simrol, 453552, India

[b]School of Physical Sciences, Indian Institute of Technology Mandi, Himachal Pradesh, 175005, India

[c]Center for Electric Vehicle and Intelligent Transport Systems, Indian Institute of Technology Indore, Simrol, 453552, India

*Corresponding author E-mail: sunil@iiti.ac.in

Abstract:

Herein, we report the enhanced electrochemical performance of a solid-state cell realized through an engineered solid electrolyte-cathode interface via a simple casting technique. The ceramic-in-polymer solid electrolyte sample with 15 wt.% NASICON-type $Li_{1.2}Sn_{0.9}Zr_{0.9}Al_{0.2}(PO_4)_3$ ceramic filler in a P(VDF-HFP) matrix (CPSE15) showed the highest room temperature conductivity of ~ 1.1×10^{-4} S cm^{-1} and lithium-ion transference number of ~ 0.60. The symmetric Li|CPSE15|Li cell showed a consistent voltage profile with an over-potential of ~ 45 mV for 750 h at a current density of 0.1 mA cm^{-2}. CPSE15 slurry was directly cast onto the $LiFePO_4$ (LFP) cathode layer using a doctor-blade coating method to obtain a cathode-electrolyte assembly. Subsequently, a full cell fabricated using this assembly and lithium metal delivered an initial discharge capacity of ~ 157 mAh g^{-1} at 0.2C. Further, the cell exhibited ~ 90 mAh g^{-1} discharge capacity at 1C and sustained 500 charge-discharge cycles at room temperature. The engineered interface in cathode-electrolyte assembly enabled this cell to outperform its conventionally fabricated counterpart with a stacked LFP cathode sheet and freestanding CPSE15 electrolyte membrane, which was attributed to a lower interfacial resistance (~ 51%) of the former.

Keywords: Solid-state cell; NASICON; composite electrolytes; cathode-electrolyte interface; doctor-blade coating.

1. Introduction

The increasing global demand for energy, coupled with the transition from internal combustion engine vehicles to electric vehicles, has compelled global policymakers to search for highly efficient energy storage technologies. Currently, the emerging energy storage requirements exceed existing high-performance batteries' capabilities, prompting battery researchers to pursue superior battery technologies [1-3]. Over the past two decades, lithium-ion technology has dominated the rechargeable battery market for portable electronics. However, further innovation is needed to meet the specific energy requirement with an eye on the safety concerns associated with organic flammable liquid electrolytes used in state-of-the-art lithium-ion batteries [4-6]. Solid-state lithium metal batteries (SSLMBs) with non-flammable solid electrolytes are developing as the future energy storage technology to mitigate the safety issues of conventional Li-ion batteries [7]. In addition, the lithium dendrite suppression capability and a wide electrochemical stability window of solid electrolytes (SEs) allow lithium metal to be used as an anode along with a high-voltage cathode, potentially boosting the specific energy of SSLMBs [8-11]. However, high electrode-electrolyte solid-solid interfacial resistance and low room-temperature ionic conductivity of solid electrolytes hinder the commercialization of current SSLMBs [12-14].

Even though SEs such as solid polymer electrolytes could reduce electrode-electrolyte resistance, they suffer from low lithium-ion conductivities at RT, which limits their use in room-temperature SSLMBs [15]. On the other hand, Inorganic SEs like thio-LISICONs and Li-Argyrodites have high Li-ion conductivities (surpassing even liquid electrolytes in effective lithium-ion conduction) but give rise to high electrode-electrolyte interfacial resistance and have poor processability [16, 17]. Hence, Ceramic-polymer composite electrolytes, which leverage the advantages of both these components, could be ideal for SSLMBs [18-22].

Composite solid electrolytes are categorized into ceramic-in-polymer solid electrolytes (CPSEs) (comprising a higher percentage of ceramics) and polymer-in-ceramic solid electrolytes (PCSEs) (comprising polymers infused in dominating ceramic matrices). In addition to boosting mechanical strength, ceramic fillers act as plasticizers to facilitate the mobility of the polymer chain for facile Li^+ migration by reducing the polymer's crystallinity while providing an additional lithium-ion conduction path (in the case of active fillers) [23-30]. The poor performance of various SSLMBs at room temperature is attributed to the cathode-electrolyte interface and low lithium-ion diffusion kinetics on the cathode side, which result in drastic specific capacity degradation at higher current densities [31]. Accordingly, the low-cost cathode-electrolyte interfacial design and the ceramic fillers' bulk lithium-ion conductivity are prominent in developing SSLMBs using CPSEs [32-34]. Substitution by aliovalent and iso-valent elements has been a proven successful strategy to facilitate the vacancy-hopping mechanism-driven Li^+ migration in NASICON-based materials by increasing the lithium concentration and decreasing the energy barrier for Li^+ conduction [35-47].

Al substitution at M-site in lithium-ion conducting NASICON-based rhombohedral $LiGe_2(PO_4)_3$ and $LiTi_2(PO_4)_3$ are extensively studied and show bulk Li^+ conductivity > 10^{-4} S cm^{-1}. The introduction of Sn for Zr in $LiZr_2(PO_4)_3$ stabilized the rhombohedral phase at much lower temperature to ~ 1000 ºC and the $LiSnZr(PO_4)_3$ exhibited bulk lithium-ion conductivity ~ 10^{-4} S cm^{-1}, as reported earlier [38]. Accordingly, Al-substitution in $LiSnZr(PO_4)_3$ compound was investigated to achieve further higher lithium-ion conductivity. The composition $Li_{1.2}Sn_{0.9}Zr_{0.9}Al_{0.2}(PO_4)_3$ [LSZAP] with a bulk ionic conductivity of ~ 1.65×10^{-4} S cm^{-1} was synthesized at 1050 ºC. P(VDF-HFP) based CPSEs with different weight fractions of LSZAP powders acting as the bifunctional plasticizer, providing extra lithium-ion conduction pathways, and decreasing the crystallinity of polymers, were fabricated with the highest ionic conductivity of ~ 1.1×10^{-4} S cm^{-1}. To mitigate the dominant cathode-electrolyte interfacial resistance in SSLMBs, a cost-effective and easily scalable coating method was adopted to design a facile cathode-electrolyte interface and the electrochemical performance of the fabricated SSLMBs with lithium metal as the anode and $LiFePO_4$ as the cathode is demonstrated (schematic shown in Fig. 1).

2. Experimental Section

2.1. Synthesis of LSZAP

$Li_{1.2}Sn_{0.9}Zr_{0.9}Al_{0.2}(PO_4)_3$ [LSZAP] was synthesized by the sol-gel technique. Lithium acetate dihydrate ($CH_3COOLi{\cdot}2H_2O$), tin (IV) chloride pentahydrate ($SnCl_4{\cdot}5H_2O$), zirconium oxychloride octahydrate ($ZrOCl_2{\cdot}8H_2O$), aluminium nitrate nonahydrate ($Al(NO_3)_3{\cdot}9H_2O$), and ammonium dihydrogen phosphate ($NH_4{\cdot}H_2PO_4$) were weighed stoichiometrically (extra 10% lithium precursor was taken). After stirring the precursors in deionized water for 10 h, citric acid and ethylene glycol were added, followed by another 6 h of stirring at room temperature. The solution was then heated to produce a gel and was ground using a mortar and pestle. After heating the mixture at 600 °C (12 h), it was cooled to room temperature. Then again heating at 750 °C (12 h), the powder was pressed into a pellet at room temperature and was then calcinated (reactive sintering) at 1050 °C for 15 h while being covered with the sacrificial powder of the same composition to minimize lithium loss.

2.2. Fabrication of ceramic-in-polymer solid electrolytes

Preparation of the CPSE membrane involved dissolving P(VDF-HFP) polymer and LiTFSI salt in DMF solvent in a weight ratio of 2.5: 1. The LSZAP powder was then dispersed into the solution at different wt. ratios, to obtain ceramic-polymer composite solutions (denoted as CPSEx; $x = 0, 5, 10, 15,$ and 20 wt. percentages of LSZAP filler). The viscous mixture was thoroughly stirred, drop cast on a petri dish, and heated under vacuum for 36 h at 50 °C to obtain the required CPSE membrane.

2.3. Designing of hybrid cathode-electrolyte assembly

The cathode slurry was prepared using 80 wt.% $LiFePO_4$ (LFP) powder, 10 wt.% Ketjen black, and 10 wt.% polystyrene-block-poly(ethylene-ran-butylene)-block-polystyrene (SEBS) binder uniformly mixed in Xylene. The slurry was coated onto aluminium foil, followed by vacuum drying at 80 °C for 12 h**.** The hybrid cathode-electrolyte assembly was then obtained by casting the composite electrolyte slurry on the dried LFP cathode (as shown in Fig. 1), followed by drying at 60 °C (36 h).

2.4. Fabrication of Coin Cells

Li|CPSE15(S)|$LiFePO_4$ and **Li|CPSE15(L)|$LiFePO_4$** cells were fabricated by sandwiching CPSE15 film between lithium metal and $LiFePO_4$ cathode sheet in CR2032 coin cells. A 5 µL drop of liquid electrolyte (1.0 M $LiPF_6$ in EC: DMC) was added at the LFP-CPSE15 interface in the **Li|CPSE15(L)|$LiFePO_4$** cell. The hybrid cathode-electrolyte assembly was used to fabricate the all-solid-state lithium metal cell with LFP as the cathode material, hereafter referred to as **Li|CPSE15(C)|$LiFePO_4$** cell.

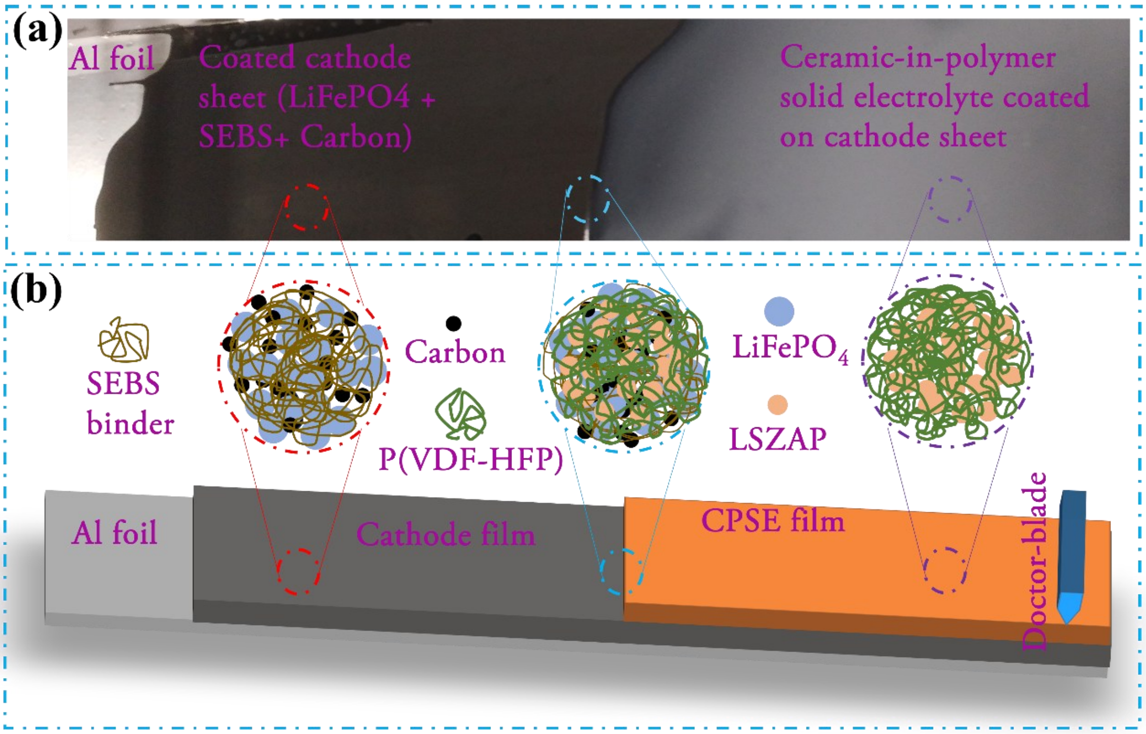

Figure 1: (a) Photograph of as-cast cathode-electrolyte assembly and (b) Schematic of doctor-blade coating of composite electrolyte onto cathode sheet.

2.5. Characterizations

The phase confirmation of ceramic $Li_{1.2}Sn_{0.9}Zr_{0.9}Al_{0.2}(PO_4)_3$ (LSZAP), polymer-salt complexes, and composite membranes was accomplished through X-ray diffraction (XRD) analysis. Empyrean (Malvern Panalytical) x-ray diffractometer with Cu-Kα radiation (operating at 40 kV, 200 mA) covered the 2θ range of 10° to 60° with a step size of ~ 0.013° for XRD data collection. The XRD data was analyzed using Rietveld refinement using Topas (version 6) [48]. Microstructure and elemental distribution of composite electrolyte membranes were assessed using a JSM field emission scanning microscope (FESEM, model JEOL-7610+). Raman spectra were obtained using a 633 nm laser beam (~ 2 mW) incident on the sample surface using a 50× LWD objective in LabRam HR-Evolution within a 100 – 1500 cm^{-1} range. Complex impedance measurements were conducted on sintered LSZAP pellets (with silver electrodes on both sides), SS|CPSE*x*|SS, Li|CPSEx|Li, Li|CPSE15(C)|$LiFePO_4$, and

Li|CPSE15(S)|$LiFePO_4$ cells using an NF (Model: ZM2376) LCR meter and a 10 mV or 100 mV signal. A cryogenic setup with Lake Shore Cryotronics was employed for precise temperature control impedance measurements. Keithley Source Meter Unit (model 2450-EC) was utilized for cyclic voltammetry (CV) and DC polarisation tests in Li|CPSE*x*|Li cells and Li|CPSE15(C)|$LiFePO_4$, as well as linear sweep voltammetry (LSV) in Li|CPSE*x*|SS with Li-electrodes and stainless-steel (SS) electrodes at 25 ºC (RT). Room temperature Galvanostatic Charge-Discharge tests were conducted on Li|CPSE*x*|Li, Li|CPSE15(C)|$LiFePO_4$, and Li|CPSE15(S)|$LiFePO_4$ cells.

3. Results and discussions

3.1. XRD analysis

The crystallographic parameters of the LSZAP powder sample were confirmed through the Rietveld refinement of the XRD pattern (Fig. 2). LSZAP was found to crystalize in a rhombohedral structure ($R\bar{3}c$ space group) with $a = b = 8.7360(7)$ Å and $c = 21.821(1)$ Å. The structural parameters of LSZAP obtained after Rietveld refinement are tabulated in Table 1. Fig. 2(b) illustrates the rhombohedral crystal structure of LSZP[$LiSnZr(PO_4)_3$] & LSZAP[$Li_{1.2}Sn_{0.9}Zr_{0.9}Al_{0.2}(PO_4)_3$] and Li^+ pathway in the rhombohedral NASICON type LSZAP crystal structure.

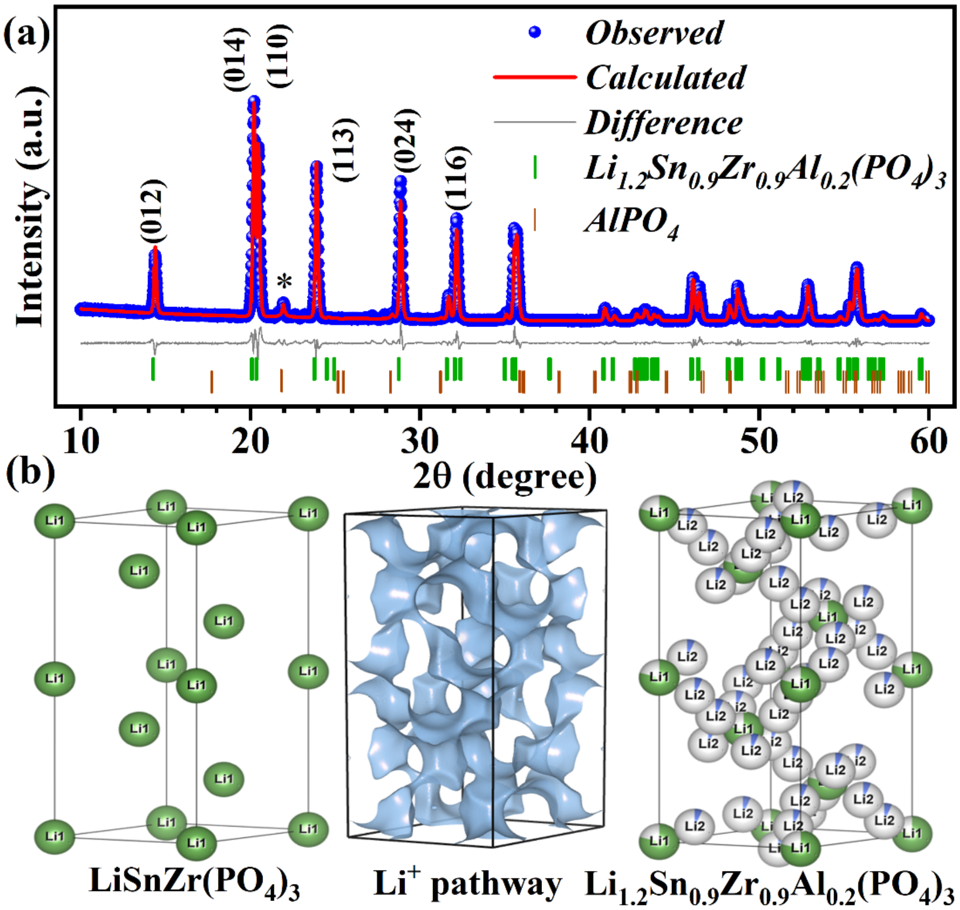

Figure 2: (a)Powder XRD data (solid dark blue balls) for $Li_{1.2}Sn_{0.9}Zr_{0.9}Al_{0.2}(PO_4)_3$ [LSZAP] calcined at 1050 °C for 15 h. The calculated pattern and the difference curves are presented as a thick red line and a thin gray line. Green vertical bars and light wine bars at the bottom depict the calculated Bragg positions for LSZAP and $AlPO_4$, respectively. (b) present the rhombohedral crystal structure of LSZP [$LiSnZr(PO_4)_3$] & LSZAP [$Li_{1.2}Sn_{0.9}Zr_{0.9}Al_{0.2}(PO_4)_3$] and Li^+ pathway in the rhombohedral NASICON type LSZAP crystal structure.

As reported in literature, the isovalent substitution of Zr with Sn in equal proportion stabilizes the rhombohedral structure of $LiSnZr(PO_4)_3$ (LSZP) at a significantly lower calcination temperature of 1000 ºC (calcination temperature of $LiZr_2(PO_4)_3$ ~ 1250 ºC) due to disorderliness caused by the difference in ionic radii at octahedral coordination sites (difference in ionic radii of Sn^{+4} & Zr^{+4} = 0.07 Å) [38].

Using the *ab initio* molecular dynamics investigations, the elevated ionic conductivity observed in Li-rich NASICON-type electrolytes has been attributed to a phenomenon termed the "pushing-out" mechanism [49]. Essentially, when an extra lithium ion is introduced, the intense coulombic repulsion between positively charged lithium ions initiates a distinctive sequence.

The introduced lithium-ion encounters a repulsive force, compelling it to move away from nearby lithium ions. This force surpasses the binding energy that holds the neighbouring lithium ion in place, leading to its displacement from its original position. Interestingly, the displaced lithium-ion is then subjected to the same electrostatic repulsion from its neighbouring ions. This results in a cascading effect where the ion is effectively "pushed out" from its initial position. Various reports also suggest a concerted lithium-ion conduction mechanism in the superionic conductors [49, 50].

In $LiSnZr(PO_4)_3$ (LSZP), the occupancy of lithium at the 6b site was 1, but in $Li_{1.2}Sn_{0.9}Zr_{0.9}Al_{0.2}(PO_4)_3$ (LSZAP), additional lithium introduced for charge compensation is redistributed from the 6b site to the 36f site as evidenced by the Rietveld refinement of XRD data (Fig. 2). The redistribution reduces the Li-Li repulsions, resulting a decrease in Li-O_6 polyhedral volume in LSZAP (15.209 $Å^3$) compared to that of LSZP (15.712 $Å^3$) [35, 38]. Lithium-ion conduction in rhombohedral NASICON materials occurs through 6b, 18e, and 36f positions of lithium sites. The three-dimensional lithium-ion migration pathway in LSZAP was obtained using softBV [51-53]. The schematic in Fig. 2 illustrates the lithium-ion conduction pathway generated using the CIF file of LSZAP created during crystal structure refinement [54]. While a decrease in Li-O_6 polyhedron volume could decrease the bottleneck size, the higher lithium concentration in the unit cell would increase the lithium-ion conduction. Therefore, a strong interplay exists between polyhedral volume and effective lithium concentration to provide maximum ionic conductivity and low activation energy. Fig. 3(a) compares the XRD data of CPSE0, CPSE5, CPSE10, CPSE15 and CPSE20. The broad peak around ~ 20^o in CPSE0 XRD data pertains to semi-crystallinity in P(VDF-HFP). The emergence of additional peaks belonging to the rhombohedral LSZAP in CPSE*x* (x = 5, 10, 15, and 20) confirms the successful fabrication of composite ceramic-in-polymer solid electrolytes.

By increasing the ceramic fraction in CPSEs, the characteristic x-ray diffraction peaks of LSZAP ($R\overline{3}c$) became prominent.

Table 1: *Various parameters obtained during Rietveld refinement of room temperature x-ray diffraction data of* $Li_{1.2}Sn_{0.9}Zr_{0.9}Al_{0.2}(PO_4)_3$ *powder.*

Site	Wyckoff position	x	y	z	Atom	Occupancy
Li1	6b	0	0	0	Li^{+1}	0.80
Li2	36f	0	0.25	0.5	Li^{+1}	0.067
Sn	12c	0	0	0.140(3)	Zr^{+4}	0.45
Zr	12c	0	0	0.140(3)	Sn^{+4}	0.45
Al	12c	0	0	0.140(3)	Al^{+3}	0.1
P	18e	0.291(4)	0	0.25	P^{+5}	1
O1	36f	0.189(6)	0.992(8)	0.192(3)	O^{-2}	1
O2	36f	0.187(5)	0.165(6)	0.082(2)	O^{-2}	1

3.2. Raman analysis

Raman spectroscopy was performed to analyze the effect of LiTFSI salt and multifunctional LSZAP ceramic filler incorporation in the P(VDF-HFP) based electrolyte membranes. Fig. 3(b) presents the Raman spectra of P(VDF-HFP), CPSE0, and CPSE15 in the region ranging from 100 cm^{-1} – 1500 cm^{-1} and the zoomed view of Raman spectra within the range of 730 cm^{-1} – 950 cm^{-1} is shown in Fig. 3(c). The Raman band at 795 cm^{-1} and 1426 cm^{-1} correspond to the combined effect of -CH_2 rocking & -CF_2 stretching and -CH_2 stretching & -CH_2 wagging modes in the α-phase of P(VDF-HFP), respectively, whereas the out-of-phase -CH_2 rocking and -CF_2 stretching in the β-phase of P(VDF-HFP) lead to the Raman band at 840 cm^{-1} [55, 56]. The peak at 1052 cm^{-1} signifies the crystallinity phase of P(VDF-HFP). The combined C-C symmetric stretching and C-C-C skeletal bonding modes are reflected in the peak at 873 cm^{-1} [56]. It is reported that the peak at 750 cm^{-1} in the Raman spectrum implies the strong ionic bond between the cation and anion of the LiTFSI salt [57].

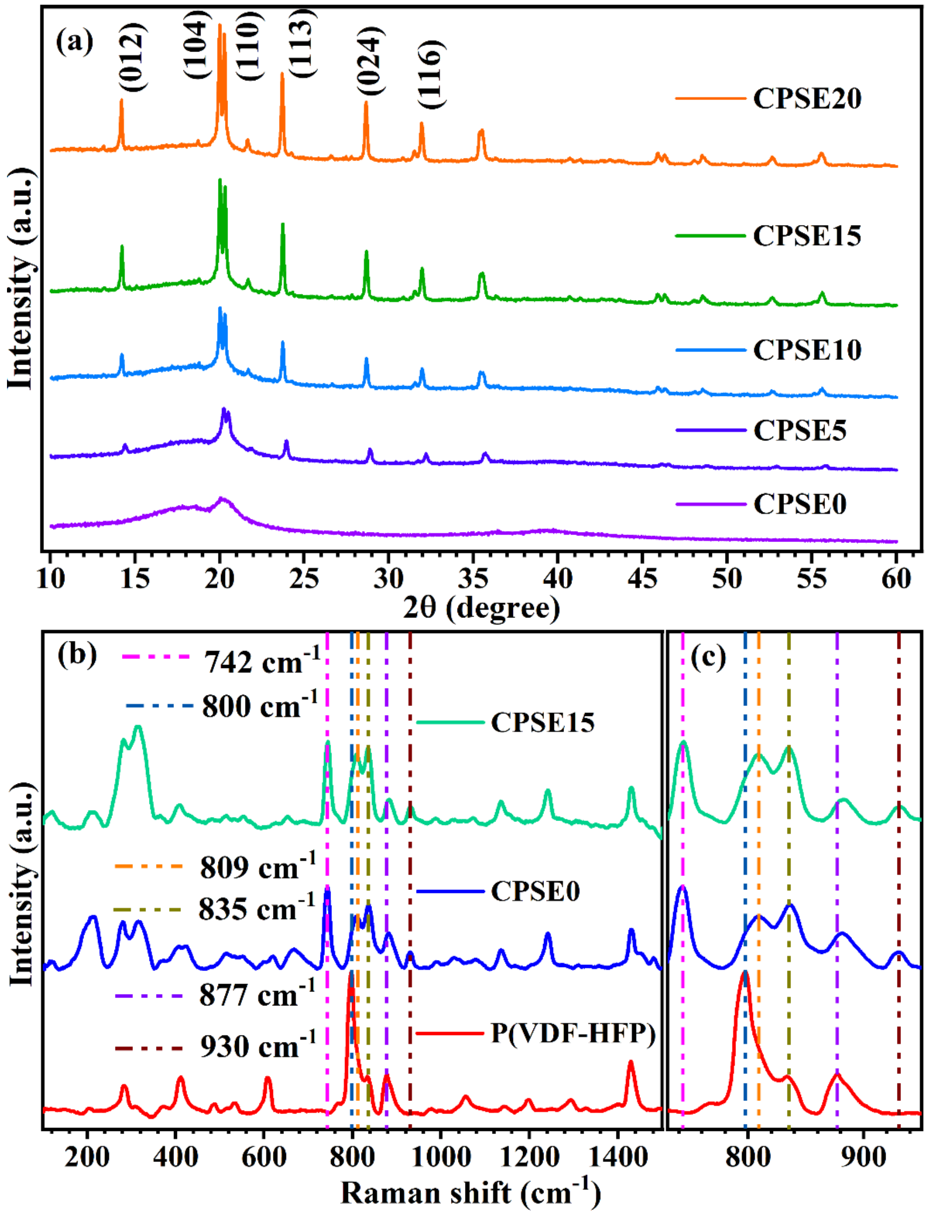

Figure 3: (a) X-ray diffraction patterns of CPSEx (x = 0, 5, 10, 15, and 20), (b) Raman spectra of P(VDF-HFP), CPSE0, and CPSE15, and (c) Zoomed view of Fig. 3(b).

The LSZAP ceramic filler acts as a Lewis acid site in reducing the crystallinity of the polymer matrix and promoting lithium salt dissociation. The intensity evolution and slight change in Raman peak positions substantiate it. The observation of all distinctive P(VDF-HFP) peaks in both CPSE0 and CPSE15 infers that the P(VDF-HFP) is chemically compatible with both LiTFSI salt and the LSZAP ceramic.

In CPSE0, the absence of a peak at 750 cm^{-1} and a peak at 742 cm^{-1} indicate salt dissociation in the P(VDF-HFP) polymer matrix. The Raman shift at 742 cm^{-1} is ascribed to the transoid conformation of $TFSI^-$ anion ($-CF_3$ groups prefer converse sides of -S-N-S- plane) [57]. In addition, the disappearance of the peak at 793 cm^{-1} and the emergence of the doublet peak at 811 cm^{-1} and 836 cm^{-1} evinces the transition from α-phase to a combination of β- and γ- phase of Poly(vinylidene fluoride-hexafluoropropylene). It is corroborated by the observed blue shift of the Raman band at 873 cm^{-1} following the introduction of LiTFSI salt [58].

3.3. Microstructure analysis

The EDS mapping of $Li_{1.2}Sn_{0.9}Zr_{0.9}(PO_4)_3$ sample is shown in Figure S1 and confirms uniform distribution of Sn, Zr, Al, and P in this sample. Figure S2 presents the SEM image and EDS mapping of CPSE15. The well-connected polymer matrix contains uniformly dispersed ceramic particles, which can be conducive to the lower activation energy of lithium-ion migration in the composite electrolyte. Figure 4 demonstrates a cross-sectional scanning electron microscopy image and the EDS mapping of the electrolyte (CPSE15) coated on the cathode (LFP). An intimate contact between the cathode and electrolyte surface was found without any visible delamination from the SEM image. EDS mapping of F, Zr, Sn, and Al confirmed the infusion of CPSE15 electrolytes into the cathode. The insolubility of SEBS binder (in DMF) used for LFP coating helped in maintaining the integrity of the LFP layer and its adhesion to the current collector while casting the electrolyte slurry on top of the cathode, evidenced by the elemental mapping of Fe given in Fig. 4(b). On the cathode side, lithium-ion conductive channels are provided by the incorporated CPSE15 electrolyte into the pores in the LFP cathode, which is expected to enhance the electrochemical performance of the hybrid cathode-electrolyte assembly.

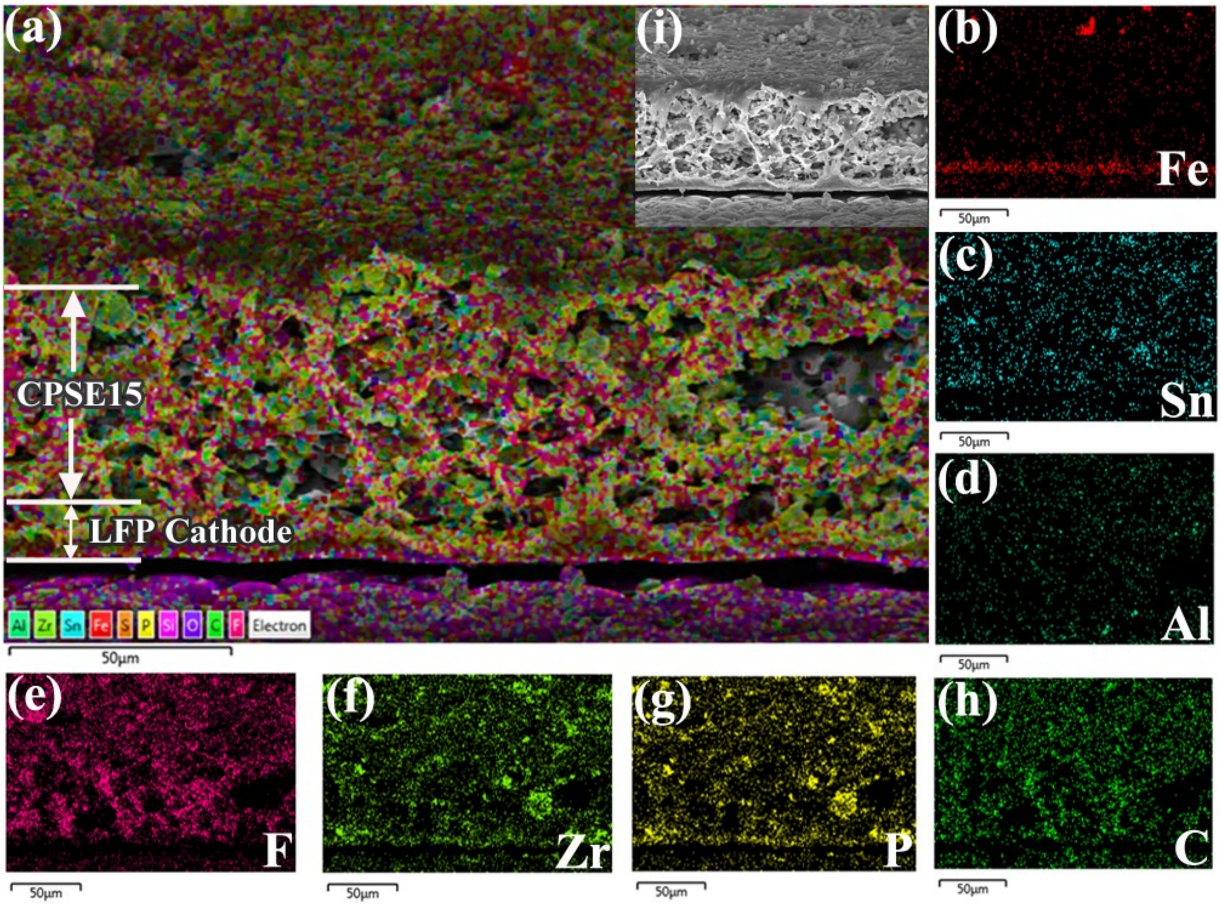

Figure 4: (a)-(h) Cross-sectional EDS mapping of CPSE15 electrolyte-LFP cathode assembly along with elemental distribution. (i) SEM image of CPSE15 electrolyte-LFP cathode interface cross-section.

3.4. Complex impedance analysis

Complex impedance analysis is a crucial method for quantifying the resistance of electrolytes by subjecting them to an appropriate AC perturbation across a broad spectrum of frequencies. Figure 5(a) shows the room temperature Nyquist plots of CPSE15 along with the equivalent circuit used to model the data. Nyquist plots for sintered LSZAP and (CPSEx) containing various LSZAP wt. percentages (x = 0, 5, 10, and 20) in the polymer backbone are given in Figs. S3 and S4.

For the LSZAP pellet, the contribution from the grain boundaries manifests as one suppressed semicircle reflecting the relaxation time in the mid-frequency band. An electrical equivalent circuit with two constant phase elements (CPEs) and two resistors (R) was used to model the experimental data (shown as the Fig. S3 inset). Here, R_g and R_{gb} correspond to grain and grain boundary resistances, respectively.

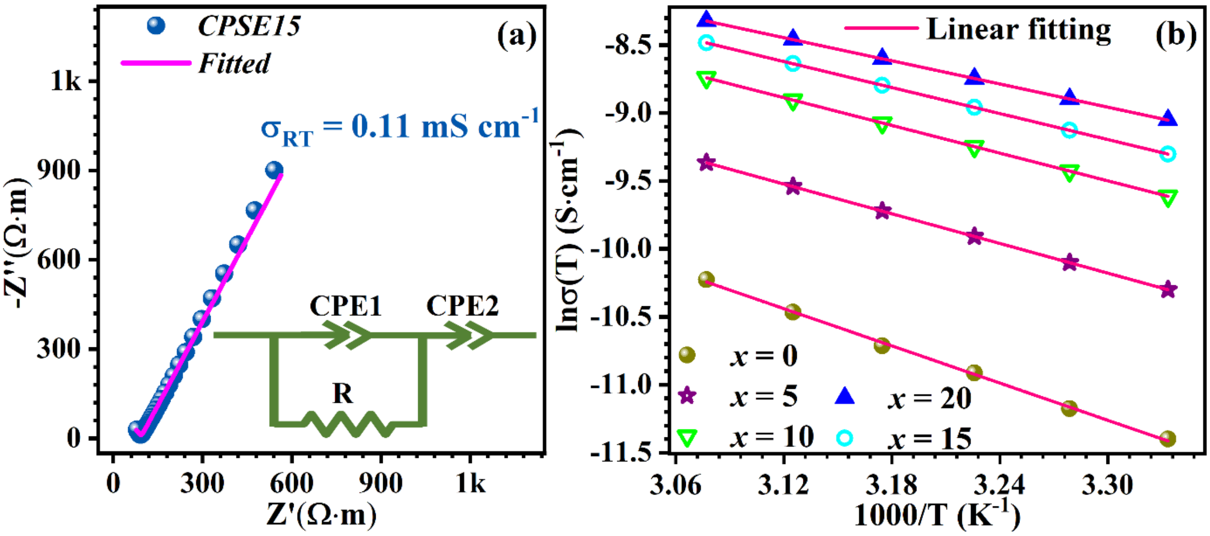

Figure 5: (a) Room temperature Nyquist plot of CPSE15 (inset present the equivalent circuit). (b) Linear fitting using Arrhenius equation for CPSEx samples.

The CPE2 indicates the lithium-ion blocking behavior of silver electrodes at lower frequencies, which causes a tail-like feature in the Nyquist plot in the low-frequency region. The fitting closely aligns with the experimental results. Calculation of bulk conductivity (σ_{RT}) employing Eq. 1,

$$\sigma_{RT} = \frac{t}{R_g \times A} \tag{1}$$

yields 1.65 × 10^{-4} S cm^{-1}, with t representing pellet thickness, R_g and A denoting grain resistance and pellet cross-sectional area, respectively.

Further, the conductivity of LSZAP at various temperatures was computed and is graphically depicted in Fig. S3(b). The linear fitting of the temperature-dependent conductivity using the Arrhenius equation (Eq. 2),

$$\sigma(T) = \sigma_0 e^{\left(\frac{-E_a}{k_B T}\right)} \tag{2}$$

wherein T, E_a, and σ_0 are absolute temperature, activation energy, and pre-exponential factor, respectively. The E_a was calculated to be 0.38 ± 0.01 eV. LSZAP exhibited higher conductivity and lower activation energy than $LiSnZr(PO_4)_3$ NASICON ceramic samples [38].

In the Nyquist plots for CPSEx samples (Fig. 5(a) and Fig. S4), a partially completed semicircle and a feature resembling a tail can be observed. This tail stems from the ion-blocking characteristics of SS electrodes in the low-frequency region, while the bulk response of the sample results in a semi-circular arc at higher frequencies. The room temperature conductivity for all samples calculated by utilizing the equivalent circuit shown in Fig. 5(a) inset is given in Table 2. As the ceramic filler concentration (x) increases up to 15%, an increase in conductivity is observed, as evidenced by the displacement of the low-frequency intercept of the semi-circular arc on the real axis of the Nyquist plot towards lower values. Maximum RT conductivity of 1.1×10^{-4} S cm^{-1} is achieved for CPSE15. In contrast, CPSE0 exhibits the lowest RT conductivity of 9.6×10^{-6} S cm^{-1} due to hindered ionic mobility within the crystalline region. The incorporation of ceramic powders in polymers is known to reduces the polymer matrix's degree of crystallinity, thus enhancing lithium-ion conduction through the amorphous phase [59-62]. A ceramic content of 15% fosters extra conduction paths for lithium-ion migration via LSZAP particles and may elevate the volume of the amorphous region in the polymer-salt matrix. It should be noted that the DMF solvent is reported to be present in PVDF-based electrolyte even after vacuum drying at 50-80 ºC. The resultant Li^+-DMF complex is shown to contribute to the high lithium-ion conduction in PVDF-based electrolytes. In this regard, such Li^+-DMF complexes may have similar role in facile Li^+ conduction in P(VDF-HFP)-based electrolytes prepared in this study.

Further, examination of temperature-dependent conductivity unveils activation energies (E_a) *via* linear fitting of the Arrhenius equation (Eq. 2) (Fig. 5(b) and Table 2). Notably, CPSE15, exhibiting maximum conductivity, showcases the lowest E_a of 0.245 ± 0.002 eV, indicating facile lithium-ion migration via the space charge region formed at the ceramic-polymer interface owing to Lewis acid-base interaction [63]. CPSE20 demonstrates reduced conductivity and elevated activation energy relative to CPSE15, which could be attributed to the increased ceramic agglomeration effects.

Table 2: *Room temperature conductivity and activation energy of CPSEx.*

Sample	Conductivity at RT (S cm^{-1})	Activation energy (eV)
CPSE0	9.6×10^{-6}	0.361 ± 0.003
CPSE5	3.1×10^{-5}	0.324 ± 0.007
CPSE10	6.2×10^{-5}	0.293 ± 0.002
CPSE15	1.1×10^{-4}	0.245 ± 0.002
CPSE20	8.5×10^{-5}	0.275 ± 0.003

3.5. Electrochemical performance

3.5.1. Cyclic voltammetry

Cyclic voltammetry (CV) testing was conducted on cells containing lithium electrodes on both sides and CPSE15 membranes as the Li-ion conducting electrolyte. The voltage range for the test was set between –1.7 V and +1.7 V, and the scan rate was 0.5 mV s^{-1}. This experiment aimed to validate the conduction of lithium ions through the solid electrolyte, and the resulting plot is given in Fig. 6(a). The peaks at ~ –0.60 V and +0.60 V confirm the facile movement of lithium ions through the CPSE15 sample. Fig. 6(b) illustrates the cyclic voltammogram for Li|CPSE15|SS in the –0.60 V to +3.5 V range at 0.5 mV s^{-1}. Similar to the symmetric cell, reduction and oxidation peaks at –0.6 V and +0.24 V, also indicate the conduction of lithium ions through the CPSE membrane. The linear increase in negative current during voltage scanning below zero potential signifies lithium stripping at Li-electrode and subsequent plating onto the steel electrode. Furthermore, the peaks that emerged between 1.2 V and 2.4 V stand for the redox reaction of chromium and iron oxides present on the stainless steel surface [64].

These cyclic voltammetry tests performed on Li|CPSE15|Li cells and Li|CPSE15|SS cells affirm the facile conduction of lithium ions through the CPSE15 material.

3.5.2. Lithium-ion transference number

The initiation of lithium dendrites' formation is known to be partially dependent on the lithium-ion transference number. A localized electric field builds up at the anode surface due to a disproportionate concentration of anion and cation driving the dendrite nucleation [65, 66]. The immobilization of anions leads to a higher lithium-ion transference number, consequently lowering the concentration gradient at the electrodes' surface. The Bruce-Vincent technique is widely employed to estimate the Li^+ transference number, which couples the DC and AC measurement techniques [67]. In our study of Li^+ transference number measurements by the Bruce-Vincent technique at 25 °C, a 50 mV DC potential was applied across the symmetric Li|CPSEx|Li cells for 3 h, after which no discernible change in current was observed. The equation used to calculate the lithium-ion transference number (t_{Li^+}) is given as,

$$t_{Li^+} = \frac{I_{ss}(\Delta \mathrm{V} - I_0 R_0)}{I_0(\Delta \mathrm{V} - I_{ss} R_{ss})} \tag{3}$$

with I_0 & I_{ss} being the initial (time = 0 h) and steady-state current (time = 3 h), and R_0 & R_{ss} representing interfacial resistances before and after DC field polarization. Fig. 7(a) illustrates the current variation for 3 h, and the figure inset presents the Nyquist plots measured before and after DC polarisation of Li|CPSE15|Li.

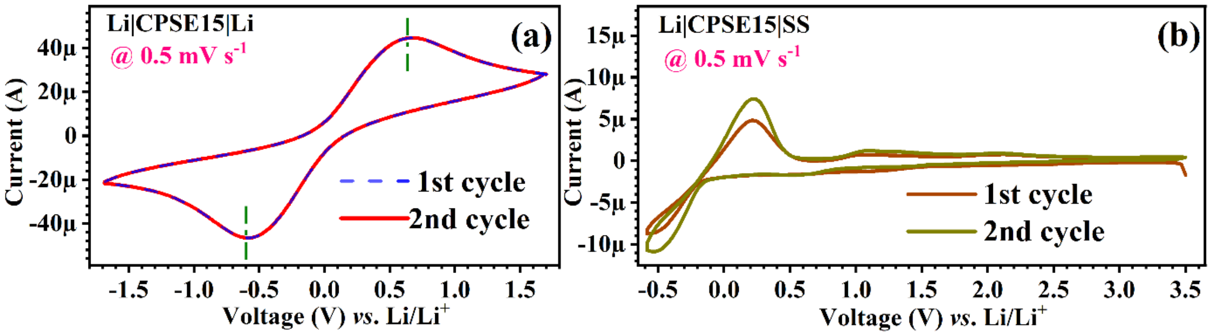

Figure 6: (a) Cyclic voltammogram of Li|CPSE15|Li cell and (b) Cyclic voltammetry on asymmetric Li|CPSE15|SS cell.

The high-frequency intercept of the semi-circular arc corresponds to the composite electrolyte resistance, while the low-frequency intercept provides the total resistance of the symmetric cell. The difference between these two resistances is the interfacial resistance. The impedance data has been fitted using an equivalent circuit (Fig. 7(a) inset). The bulk resistance of the CPSE15 electrolyte remained relatively unchanged, but the interfacial resistance increased from 219 Ω to 270 Ω after DC polarization. The t_{Li+} of CPSE*x* calculated (Eq. 3) are presented in Table 3.

Table 3: *Lithium-ion transference number (t_{Li+}) calculated for CPSE0, CPSE5, CPSE10, CPSE15, and CPSE20 (DC polarization voltage = 50 mV).*

Sample	I_0 **(μA)**	I_{ss} **(μA)**	R_0 **(Ω)**	R_{ss} **(Ω)**	t_{Li+}
CPSE0	29.20	9.20	277	675	0.30
CPSE5	27.57	11.00	262	527	0.38
CPSE10	26.40	12.50	234	382	0.45
CPSE15	22.57	13.96	219	270	0.60
CPSE20	23.56	13.10	226	304	0.54

The sample with 15 wt.% ceramic addition exhibited the maximum t_{Li+} of ~ 0.60, following a trend consistent with the ionic conductivity. Inorganic lithium-ion conductive ceramics are renowned for their high Li-ion transference numbers, often approaching 1.

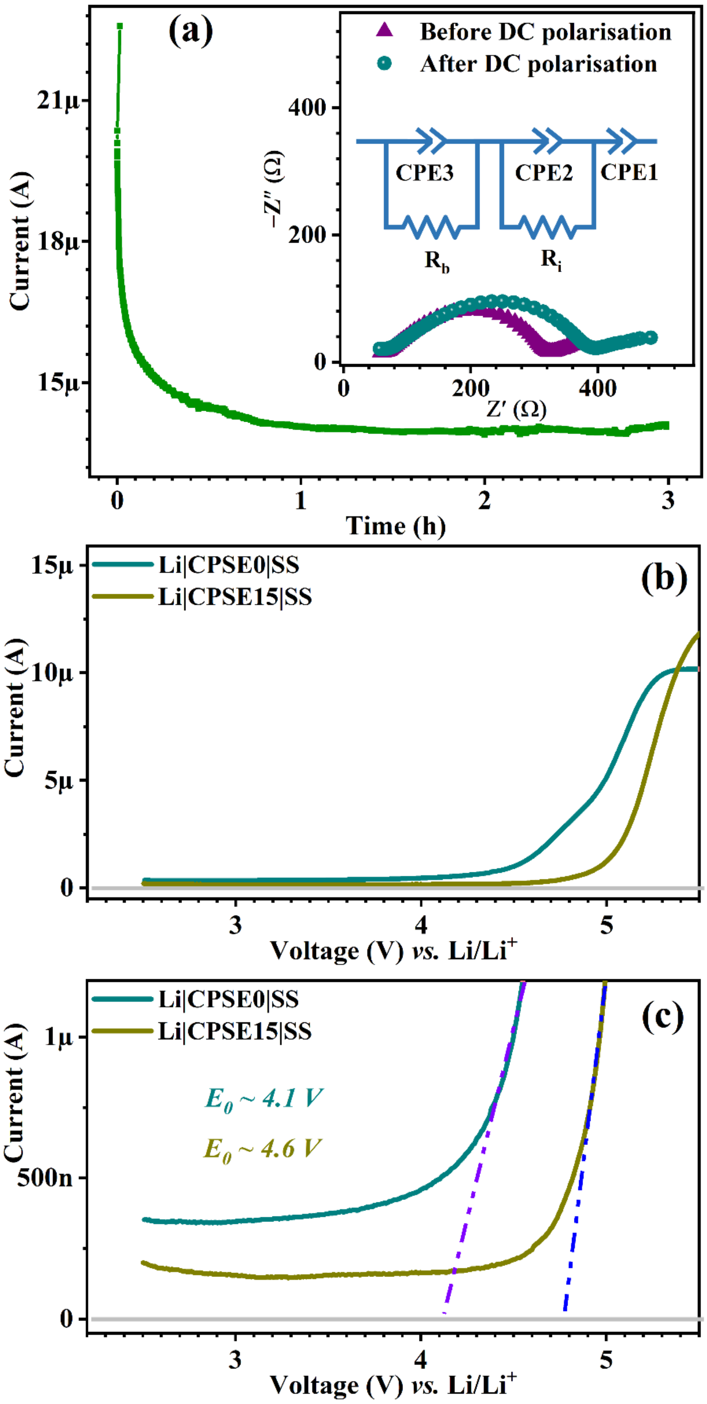

Figure 7: (a) Time variation of current under 0.05 V DC field applied to Li|CPSE15|Li cell. The inset figure displays the Nyquist plots before and after the DC polarisation, along with the corresponding equivalent circuit used to compute the interfacial resistance, (b) linear sweep voltammetry data for CPSE0 and CPSE15, and (c) shows the magnified view of the (b).

Additionally, the inclusion of NASICON fillers restricts the motion of (TFSI)$^-$ and poly-ions. As a result, the CPSE15 composite exhibits an elevated Li-ion transference number in comparison to the CPSE0 sample (t_{Li^+} = 0.30), which comprises only the polymer and salt.

Furthermore, the presence of LSZAP particles might serve as Lewis acid sites, promoting complexation between the anion part of LiTFSI salt and LSZAP. Consequently, the introduction of ceramics increases the Li^+ transference number. However, the CPSE20 electrolyte displayed a decrease in t_{Li+} compared to CPSE15. This decline can be ascribed to the aggregation of LSZAP particles. Table S2 compares the conductivity and lithium-ion transference number of CPSE15 electrolyte with other reported P(VDF-HFP)-based composite electrolytes.

3.5.3. Linear sweep voltammetry

Linear sweep voltammetry was carried out to determine the impact of ceramic filler on the electrochemical stability window (ESW) of composite solid electrolytes, and the results for CPSE0 and CPSE15 are shown in Fig. 7(b) & (c). The voltage at which the onset of the large current occurs represents the maximum value of the electrolyte's ESW. In this study, LSV was conducted on asymmetric cells using the Li|CPSE*x*|SS configuration, employing a voltage range of 2.5 V to 6 V at 0.5 mV s^{-1}. At initial voltages, a low current was observed flowing through the CPSEs; however, a much larger current onset was detected beyond a critical voltage, indicating electrolyte decomposition. The ESW was found to be ~ 4.1 V for CPSE0, where the introduction of 15 wt.% LSZAP active fillers widened the ESW of CPSE15 to ~ 4.7 V. The strong interaction of ceramic fillers and lithium salts with the polymer matrix contributed to the improved oxidative stability of the P(VDF-HFP). The broad electrochemical stability range allows the realization of high-potential cathodes like Spinel-type and Layered Oxides in conjunction with lithium metal as the anode in SSLMBs.

3.5.4 Symmetric cell GCD

The cycling performance of the Li symmetric batteries assembled with CPSE0 and CPSE15 membranes at room temperature was performed to evaluate the interfacial stability and compatibility of the electrolyte to the lithium metal electrode. Fig. 8 shows the galvanostatic charge-discharge (GCD) profiles of lithium symmetric cells with CPSE15 cells cycling at various current densities of 0.1 mA cm^{-2}, 0.2 mA cm^{-2}, 0.4 mA cm^{-2}, 0.6 mA cm^{-2}, and 0.8 mA cm^{-2} for 30 minutes of plating and 30 minutes of stripping of lithium.

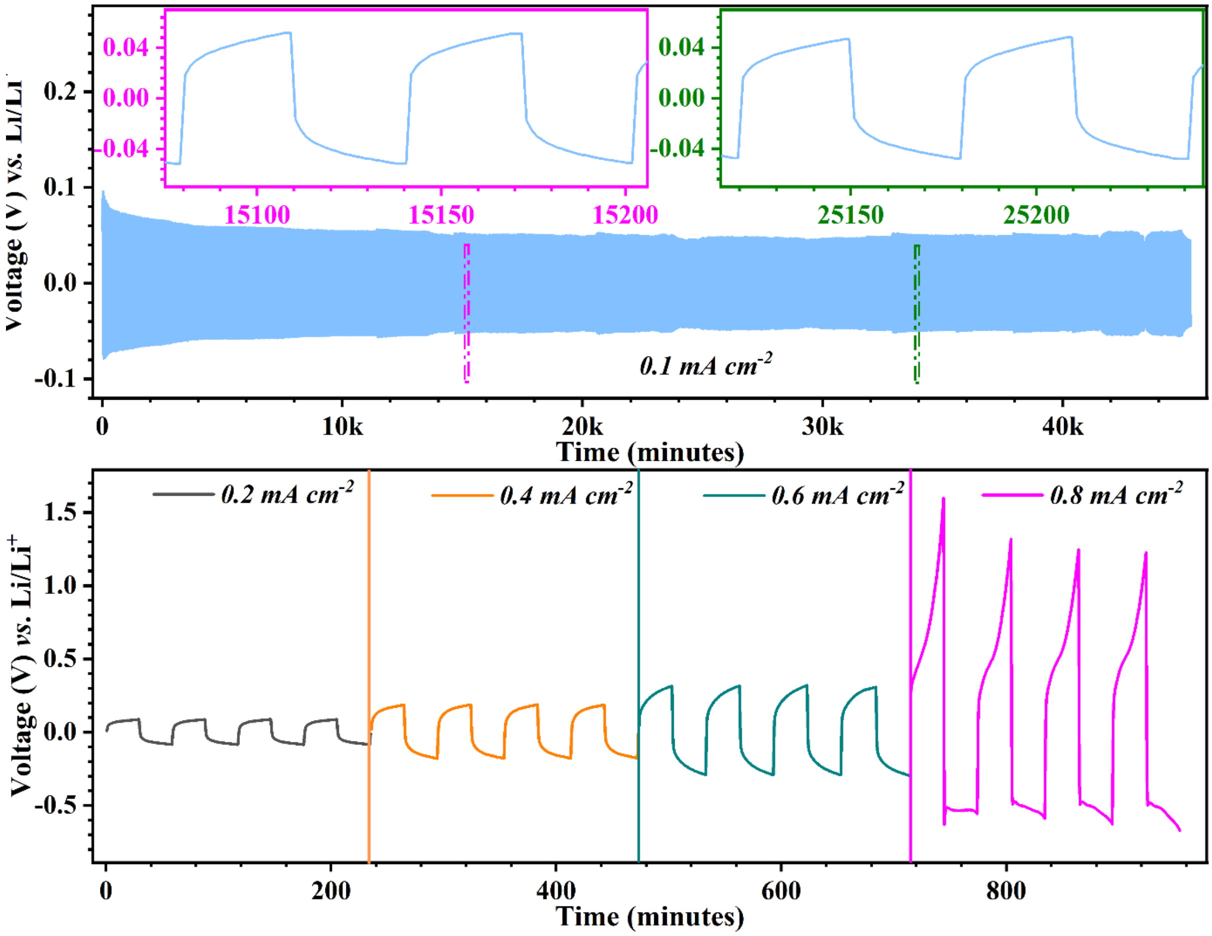

Figure 8: Galvanostatic charge-discharge plot of Li|CPSE15|Li cell.

The GCD plot of Li|CPSE0|Li cell is given in Fig. S5. The symmetric cell with CPSE0 shows larger over-potentials than its counterpart CPSE15 at a current density of 0.1 mA cm^{-2}. An erratic voltage profile in all plating-stripping cycles and a gradually increasing average overpotential with cycling are observed for lithium symmetric cells with the CPSE0 sample. Inhomogeneous current distribution at the electrode-electrolyte surface can cause the formation of dead lithium, leading to the exposure of unreacted lithium for the side reactions with the electrolyte [68-72]. So, continuous side reactions and accumulation of dead lithium could lead to a tortuous path for lithium-ion transport at the interface, which is reflected as the peaks and arcing-like features in the voltage profile of the symmetric Li|CPSE0|Li cells at 0.1 mA cm^{-2}. On the contrary, at an areal current density of 0.1 mA cm^{-2}, a relatively stable voltage profile for 750 h was observed with CPSE15 as the electrolyte membrane, indicating stable SEI formation. As discussed in the Raman section, the addition of ceramic fillers promotes more lithium salt dissociation, which may facilitate TFSI$^-$ decomposition at the lithium metal surface to form a stable lithium-ion conducting SEI layer.

3.5.5. Full cell performance

Cyclic voltammetry (CV) measurements were conducted on a full Li|CPSE15(C)|LiFePO$_4$ cell in a voltage range of 2.8 V to 4.2 V with a scan rate of 0.1 mV s^{-1} at room temperature, and the resulting plot is presented in Fig. 9(a). In Li|CPSE15(C)|LiFePO$_4$ cell, lithiation of LiFePO$_4$ occurred at ~ 3.13 V, accompanied by a corresponding delithiation peak at ~ 3.68 V. During Li$^+$ deintercalation in LiFePO$_4$, Fe changes oxidation state from +2 to +3 and intercalation is followed by reversal to +2 oxidation state.

Fig. 9(b) presents the charging-discharging profile of Li|CPSE15(C)|LiFePO$_4$ and Li|CPSE15(L)|LiFePO$_4$ at various C-rates with a lower cut-off voltage of 2.8 V and higher limiting voltage of 4.2 V at room temperature (25 ºC). Both the Li|CPSE15(C)|LiFePO$_4$ and Li|CPSE15(L)|LiFePO$_4$ delivered nearly the same specific capacity ~ 157 mAh g^{-1} at 0.2C (C rates were calculated assuming a theoretical specific capacity ~ 170 mAh g^{-1} for LiFePO$_4$). At the same time, there was a discernible difference in the voltage profiles (Fig. 9(b)). The well-known voltage plateau of the LiFePO$_4$ cathode was observed in the lithium cell fabricated with a hybrid cathode-solid electrolyte interface architecture. The deviation from the plateau behavior in the voltage curve in the Li|CPSE15(L)|LiFePO$_4$ cell can be attributed to an inferior cathode-CPSE15 interface. With an increase in the C-rate, the specific capacities in both the Li|CPSE15(C)|LiFePO$_4$ and Li|CPSE15(L)|LiFePO$_4$ cells decreased. The decreased capacities could be attributed to unutilized cathode active material owing to the limited lithium-ion conductivity of CPSE15 and interfacial impedance. At 1C, Li|CPSE15(L)|$LiFePO_4$ cell showed lesser capacity (~ 72 mAh g^{-1}) than that of the Li|CPSE15(C)|$LiFePO_4$ cell (~ 90 mAh g^{-1}). As the composite solid electrolyte slurry was cast upon the porous LFP cathode sheet for Li|CPSE15(C)|$LiFePO_4$, resulting in more lithium-ion conductive channels in the $LiFePO_4$ cathode layer, this cell outperformed its counterpart Li|CPSE15(L)|$LiFePO_4$ cell in terms of overpotential, voltage plateau, and specific capacities at 0.5C and 1C discharge rates. A comparative illustration of the specific capacities of the Li|CPSE15(C)|$LiFePO_4$ and Li|CPSE15(S)|$LiFePO_4$ is shown in Fig. S6. The stacked cell without liquid electrolyte droplet showed a lower specific capacity of ~ 130 mAh g^{-1} even at 0.2C. Further, polarization in the GCD curve for this cell is much higher (~ 730 mV) as compared to ~ 290 mV for the Li|CPSE15(C)|$LiFePO_4$ cell.

The impact of better cathode-electrolyte interface in Li|CPSE15(C)|$LiFePO_4$ cell as compared to Li|CPSE15(S)|$LiFePO_4$ is reflected in the respective Nyquist plots as demonstrated in Fig. S7. The electrode-electrolyte interface resistances calculated from the impedance data fitted using the equivalent circuit (shown as Fig. S7 inset) were found to be ~ 631 Ω and ~ 1307 Ω for Li|CPSE15(C)|$LiFePO_4$ and Li|CPSE15(S)|$LiFePO_4$ cells, respectively (Table S1).

Figure 9(c) shows the GCD cycling Li|CPSE15(C)|$LiFePO_4$ cell at 0.2C. The cell delivered an initial discharge capacity of ~ 157 mAh g^{-1} with ~ 87.26% of capacity retention after 100 cycles. The observed decline in capacity could be attributed to several factors, including the increase in electrode-electrolyte interfacial resistance due to ongoing irreversible secondary reactions. Fig. 9(d) illustrates the cyclic performance of Li|CPSE15(C)|$LiFePO_4$ cell for 500 h at 1C. The cell retains ~ 73% of its initial discharge capacity after 100 cycles and exhibits a specific capacity of about 20 mAh g^{-1} even after 500 cycles. This drastic capacity degradation after 100 cycles, compared to cycling performance at 0.2C, could be ascribed to slow electrode kinetics and accelerated irreversible energy losses because of internal cell resistance at higher currents.

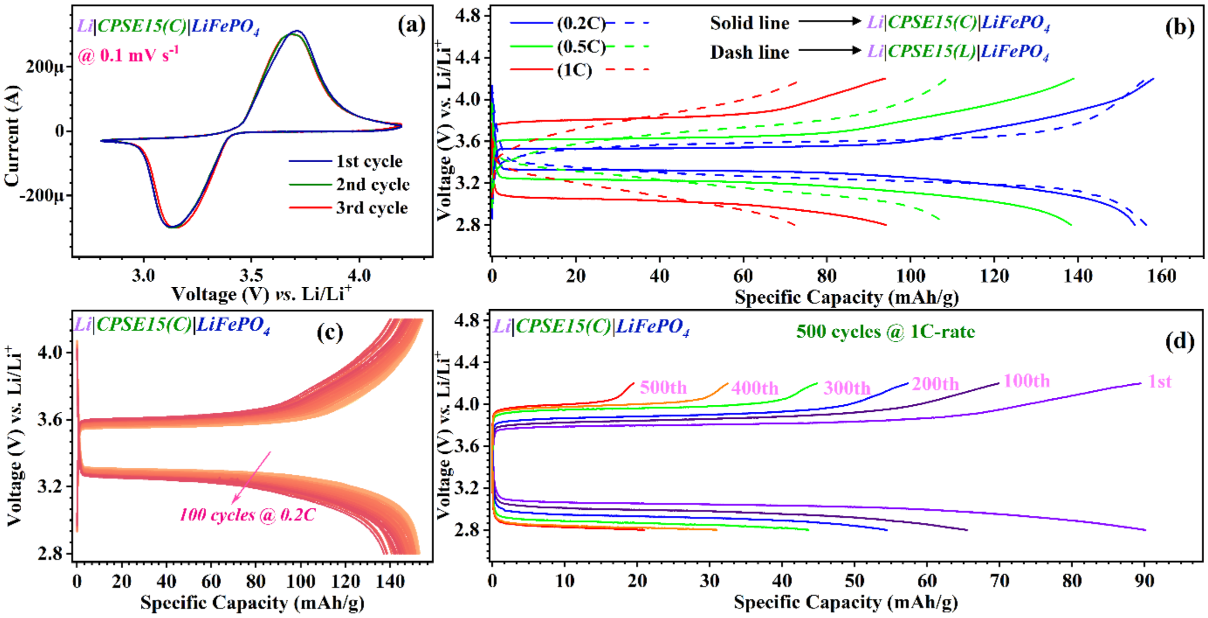

Figure 9: (a) Cyclic voltammetry of Li|CPSE15(C)|LiFePO$_4$, (b) comparison of GCD curves of Li|CPSE15(C)|LiFePO$_4$ & Li|CPSE15(L)|LiFePO$_4$ at different C-rates, (c) GCD profile of Li|CPSE15(C)|LiFePO$_4$ at 0.2C, and (d) GCD data of Li|CPSE15(C)|LiFePO$_4$ at 1C.

4. Conclusions

The ceramic-in-polymer solid electrolyte sample with 15 wt.% LSZAP ceramic powders revealed the highest room temperature ionic conductivity of ~ 1.1×10^{-4} S cm^{-1}, lowest activation energy of ~ 0.245 ± 0.002 eV, and the highest lithium-ion transference number of ~ 0.60 amongst all CPSE samples. The GCD data of Li|CPSE15|Li cell for 750 h signifies the durability and long cycle stability with an overpotential of ~ 45 mV at a current density of 0.1 mA cm^{-2}. The critical current density was estimated to be 0.6 mA cm^{-2}. The full Li|CPSE15(C)|LiFePO$_4$ cell fabricated delivered an initial discharge capacity of ~ 157 mAh g^{-1} with ~ 87.3% capacity retention after 100 cycles at 0.2C. Further, this cell exhibited long-run stability for more than 500 cycles at 1C. The enhanced rate performance of Li|CPSE15(C)|LiFePO$_4$ compared to Li|CPSE15(L)|LiFePO$_4$ signifies the importance of facile electrolyte-cathode interface design. A simple doctor blade coating technique with appropriate solvent selection to prepare cathode/composite-solid-electrolyte bi-layers demonstrated in this work would pave the way to the commercialization of all-solid-state lithium metal batteries.

Conflicts of interest:

There are no conflicts to declare.

Data availability:

Data will be made available on request.

Acknowledgements:

The authors gratefully acknowledge the Science and Engineering Research Board (SERB), Government of India (Grant No. CRG/2021/005548) and Department of Science and Technology (DST), Government of India (Grant No. DST/TMD/IC-MAP/2K20/01). The author (AKD) thanks the Ministry of Education, Government of India, for the Prime Ministers Research Fellowship (PMRF) (PMRF ID - 2102737).

Credit author statement

Asish Kumar Das: Conceptualisation, Methodology, Investigation, Funding acquisition, Writing - Original Draft; **Manish Badole:** Writing - Review & Editing; **Hari Narayanan Vasavan:** Writing - Review & Editing; **Samriddhi Saxena:** Writing - Review & Editing; **Pratiksha Gami:** Writing - Review & Editing; **Sonia Deswal:** Writing - Review & Editing; **Pradeep Kumar:** Writing - Review & Editing; **Sunil Kumar:** Conceptualisation, Methodology, Funding acquisition, Supervision, Resources, Project administration, Validation, Writing - Review & Editing.

References:

[1] J.B. Goodenough, K.-S. Park, The Li-Ion Rechargeable Battery: A Perspective, J. Am. Chem. Soc., 135 (2013) 1167 https://doi.org/10.1021/ja3091438

[2] B. Diouf, R. Pode, Potential of lithium-ion batteries in renewable energy, Renew. Energ., 76 (2015) 375 https://doi.org/10.1016/j.renene.2014.11.058

[3] E.C. Evarts, Lithium batteries: To the limits of lithium, Nature, 526 (2015) S93 https://doi.org/10.1038/526S93a

[4] H.N. Vasavan, M. Badole, S. Saxena, A.K. Das, S. Deswal, P. Kumar, S. Kumar, Excellent Structural Stability-Driven Cyclability in P2-Type Ti-Based Cathode for Na-Ion Batteries, ACS Appl. Energy Mater., 6 (2023) 2440-2447 https://doi.org/10.1021/acsaem.2c03750

[5] S. Saxena, H.N. Vasavan, M. Badole, A.K. Das, S. Deswal, P. Kumar, S. Kumar, Tailored P2/O3 phase-dependent electrochemical behavior of Mn-based cathode for sodium-ion batteries, J. Energy Storage, 64 (2023) https://doi.org/10.1016/j.est.2023.107242

[6] S. Megahed, W. Ebner, Lithium-ion battery for electronic applications, J. Power Sources, 54 (1995) 155 https://doi.org/10.1016/0378-7753(94)02059-C

[7] R. Song, J. Yao, R. Xu, Z. Li, X. Yan, C. Yu, Z. Huang, L. Zhang, Metastable Decomposition Realizing Dendrite-Free Solid-State Li Metal Batteries, Adv. Energy Mater., 13 (2023) 2203631 https://doi.org/10.1002/aenm.202203631

[8] N. Nitta, F. Wu, J.T. Lee, G. Yushin, Li-ion battery materials: present and future, Mater. Today, 18 (2015) 252 https://doi.org/10.1016/j.mattod.2014.10.040

[9] L. Li, J. Yao, R. Xu, Q. Lin, X. Yan, C. Yu, L. Zhang, Highly stable and encapsulation-microstructural cathode derived by self-pressurization behavior in Na-halides-based all-solid-state batteries, Energy Storage Mater., 63 (2023) 103016 https://doi.org/10.1016/j.ensm.2023.103016

[10] S. Chen, C. Yu, C. Wei, Z. Jiang, Z. Zhang, L. Peng, S. Cheng, J. Xie, Unraveling Electrochemical Stability and Reversible Redox of Y-Doped Li_2ZrCl_6 Solid Electrolytes, Energy Mater. Adv., 4 (2023) 0019 https://doi.org/10.34133/energymatadv.0019

[11] D. Zeng, J. Yao, L. Zhang, R. Xu, S. Wang, X. Yan, C. Yu, L. Wang, Promoting favorable interfacial properties in lithium-based batteries using chlorine-rich sulfide inorganic solid-state electrolytes, Nat. Commun., 13 (2022) 1909 https://doi.org/10.1038/s41467-022-29596-8

[12] C. Li, X. Zhang, Z. Yang, H. Lv, T. Song, S. Lu, Y. Zhang, T. Yang, F. Xu, F. Wu, D. Mu, Stable cycling of $LiNi_{0.9}Co_{0.05}Mn_{0.05}O_2$/lithium metal batteries enabled by synergistic tuning the surface stability of cathode/anode, J. Energy Chem., 87 (2023) 342-350 https://doi.org/10.1016/j.jechem.2023.08.033

[13] R. Guo, W. Han, The effects of electrolytes, electrolyte/electrode interphase, and binders on lithium-ion batteries at low temperature, Mater. Today Sustain., 19 (2022) 100187 https://doi.org/10.1016/j.mtsust.2022.100187

[14] T. Kim, Voltage-dependent formation of cathode–electrolyte interphase with independent metallic layer in $LiNi_{0.8}Mn_{0.1}Co_{0.1}O_2$ cathode for high-energy density lithium-ion batteries, Mater. Today Sustain., 21 (2023) 100326 https://doi.org/10.1016/j.mtsust.2023.100326

[15] S. Jian, Y. Cao, W. Feng, G. Yin, Y. Zhao, Y. Lai, T. Zhang, X. Ling, H. Wu, H. Bi, Y. Dong, Recent progress in solid polymer electrolytes with various dimensional fillers: a review, Mater. Today Sustain., 20 (2022) 100224 https://doi.org/10.1016/j.mtsust.2022.100224

[16] X. Zhao, P. Xiang, J. Wu, Z. Liu, L. Shen, G. Liu, Z. Tian, L. Chen, X. Yao, Toluene Tolerated $Li_{9.88}GeP_{1.96}Sb_{0.04}S_{11.88}Cl_{0.12}$ Solid Electrolyte toward Ultrathin Membranes for All-Solid-State Lithium Batteries, Nano Lett., 23 (2023) 227-234 https://doi.org/10.1021/acs.nanolett.2c04140

[17] P. Yu, N. Ahmad, J. Yang, C. Zeng, X. Liang, W. Huang, M. Ni, P. Mao, W. Yang, Dual-doping for enhancing chemical stability of functional anionic units in sulfide for high-performance all-solid-state lithium batteries, J. Energy Chem., 86 (2023) 382-390 https://doi.org/10.1016/j.jechem.2023.07.038

[18] X. Yu, A. Manthiram, A review of composite polymer-ceramic electrolytes for lithium batteries, Energy Storage Mater., 34 (2021) 282-300 https://doi.org/10.1016/j.ensm.2020.10.006

[19] H. Jeon, H.A. Hoang, D. Kim, Flexible PVA/BMIMOTf/LLZTO composite electrolyte with liquid-comparable ionic conductivity for solid-state lithium metal battery, J. Energy Chem., 74 (2022) 128-139 https://doi.org/10.1016/j.jechem.2022.07.014

[20] T. Huang, W. Xiong, X. Ye, Z. Huang, Y. Feng, J. Liang, S. Ye, J. Piao, X. Wang, Y. Li, X. Ren, C. Chen, S. Huang, X. Ouyang, Q. Zhang, J. Liu, A cerium-doped NASICON chemically coupled poly(vinylidene fluoride-hexafluoropropylene)-based polymer electrolyte for high-rate and high-voltage quasi-solid-state lithium metal batteries, J. Energy Chem., 73 (2022) 311-321 https://doi.org/10.1016/j.jechem.2022.06.030

[21] D. Kim, C. Bak, N. Kim, J. Park, M.J. Lee, D.O. Shin, Y.G. Lee, Y.M. Lee, Surface-patterned graphite electrode with hybrid polymer/garnet electrolyte for all-solid-state batteries, Mater. Today Sustain., 22 (2023) 100338 https://doi.org/10.1016/j.mtsust.2023.100338

[22] Z. Zhang, X. Wang, X. Li, J. Zhao, G. Liu, W. Yu, X. Dong, J. Wang, Review on composite solid electrolytes for solid-state lithium-ion batteries, Mater. Today Sustain., 21 (2023) 100316 https://doi.org/10.1016/j.mtsust.2023.100316

[23] X. Zhang, T. Liu, S. Zhang, X. Huang, B. Xu, Y. Lin, B. Xu, L. Li, C.-W. Nan, Y. Shen, Synergistic Coupling between $Li_{6.75}La_3Zr_{1.75}Ta_{0.25}O_{12}$ and Poly(vinylidene fluoride) Induces High Ionic Conductivity, Mechanical Strength, and Thermal Stability of Solid Composite Electrolytes, J. Am. Chem. Soc., 139 (2017) 13779-13785 https://doi.org/10.1021/jacs.7b06364

[24] S. Choudhary, R.J. Sengwa, Effects of different inorganic nanoparticles on the structural, dielectric and ion transportation properties of polymers blend based nanocomposite solid polymer electrolytes, Electrochim. Acta, 247 (2017) 924-941 https://doi.org/10.1016/j.electacta.2017.07.051

[25] B. Luo, W. Wang, Q. Wang, W. Ji, G. Yu, Z. Liu, Z. Zhao, X. Wang, S. Wang, J. Zhang, Facilitating ionic conductivity and interfacial stability via oxygen vacancies-enriched TiO_2 microrods for composite polymer electrolytes, Chem. Eng. J., 460 (2023) 141329 https://doi.org/10.1016/j.cej.2023.141329

[26] K. Khan, B. Fu, H. Xin, B.A. Beshiwork, M.B. Hanif, J. Wu, Z. Fang, J. Yang, T. Li, C. Chen, M. Motola, Z. Xu, M. Wu, Composite polymer electrolyte incorporating WO_3 nanofillers with enhanced performance for dendrite-free solid-state lithium battery, Ceram. Int., 49 (2023) 4473-4481 https://doi.org/10.1016/j.ceramint.2022.09.333

[27] T. Yang, J. Zheng, Q. Cheng, Y.-Y. Hu, C.K. Chan, Composite Polymer Electrolytes with $Li_7La_3Zr_2O_{12}$ Garnet-Type Nanowires as Ceramic Fillers: Mechanism of Conductivity

Enhancement and Role of Doping and Morphology, ACS Appl. Mater. Interfaces, 9 (2017) 21773-21780 https://doi.org/10.1021/acsami.7b03806

[28] P. Sivaraj, K.P. Abhilash, B. Nalini, P. Perumal, P.C. Selvin, Free-standing, high Li-ion conducting hybrid PAN/PVdF/$LiClO_4$/$Li_{0.5}La_{0.5}TiO_3$ nanocomposite solid polymer electrolytes for all-solid-state batteries, J. Solid State Electrochem., 25 (2021) 905-917 https://doi.org/10.1007/s10008-020-04858-x

[29] B.-J. Sung, P.N. Didwal, R. Verma, A.-G. Nguyen, D.R. Chang, C.-J. Park, Composite solid electrolyte comprising poly(propylene carbonate) and $Li_{1.5}Al_{0.5}Ge_{1.5}(PO_4)_3$ for long-life all-solid-state Li-ion batteries, Electrochim. Acta, 392 (2021) 139007 https://doi.org/10.1016/j.electacta.2021.139007

[30] S. Li, J. Lu, Z. Geng, Y. Chen, X. Yu, M. He, H. Li, Solid Polymer Electrolyte Reinforced with a $Li_{1.3}Al_{0.3}Ti_{1.7}(PO_4)_3$-Coated Separator for All-Solid-State Lithium Batteries, ACS Appl. Mater. Interfaces, 14 (2022) 1195-1202 https://doi.org/10.1021/acsami.1c21804

[31] X. Lu, Y. Wang, X. Xu, B. Yan, T. Wu, L. Lu, Polymer-Based Solid-State Electrolytes for High-Energy-Density Lithium-Ion Batteries – Review, Adv. Energy Mater., 13 (2023) 2301746 https://doi.org/10.1002/aenm.202301746

[32] L. Liu, D. Zhang, T. Yang, W. Hu, X. Meng, J. Mo, W. Hou, Q. Fan, K. Liu, B. Jiang, L. Chu, M. Li, Flexible ion-conducting membranes with 3D continuous nanohybrid networks for high-performance solid-state metallic lithium batteries, J. Energy Chem., 75 (2022) 360-368 https://doi.org/10.1016/j.jechem.2022.08.036

[33] L. Zhai, K. Yang, F. Jiang, W. Liu, Z. Yan, J. Sun, High-performance solid-state lithium metal batteries achieved by interface modification, J. Energy Chem., 79 (2023) 357-364 https://doi.org/10.1016/j.jechem.2023.01.022

[34] H. Yan, J. Yao, Z. Ye, Q. Lin, Z. Zhang, S. Li, D. Song, Z. Wang, C. Yu, L. Zhang, Al-F co-doping towards enhanced electrolyte-electrodes interface properties for halide and sulfide solid electrolytes, Chin. Chem. Lett., (2024) 109568 https://doi.org/10.1016/j.cclet.2024.109568

[35] T. Pareek, B. Singh, S. Dwivedi, A.K. Yadav, Anita, S. Sen, P. Kumar, S. Kumar, Ionic conduction and vibrational characteristics of Al^{3+} modified monoclinic $LiZr_2(PO_4)_3$, Electrochim. Acta, 263 (2018) 533-543 https://doi.org/10.1016/j.electacta.2018.01.087

[36] S. Kumar, P. Balaya, Improved ionic conductivity in NASICON-type Sr^{2+} doped $LiZr_2(PO_4)_3$, Solid State Ion., 296 (2016) 1-6 https://doi.org/10.1016/j.ssi.2016.08.012

[37] S.A. Ahmed, T. Pareek, S. Dwivedi, M. Badole, S. Kumar, $LiSn_2(PO_4)_3$-based polymer-in-ceramic composite electrolyte with high ionic conductivity for all-solid-state lithium batteries, J. Solid State Electrochem., 24 (2020) 2407-2417 https://doi.org/10.1007/s10008-020-04783-z

[38] T. Pareek, S. Dwivedi, B. Singh, D. Kumar, P. Kumar, S. Kumar, $LiSnZr(PO_4)_3$: NASICON-type solid electrolyte with excellent room temperature Li^+ conductivity, J. Alloys Compd., 777 (2019) 602-611 https://doi.org/10.1016/j.jallcom.2018.10.384

[39] A.K. Das, M. Badole, H.N. Vasavan, S. Saxena, P. Gami, S. Kumar, Highly conductive ceramic-in-polymer composite electrolyte enabling superior electrochemical performance for all-solid-state lithium batteries, Ceram. Int., 49 (2023) 29719-29728 https://doi.org/10.1016/j.ceramint.2023.06.214

[40] A. Loutati, P. Odenwald, B. Aktekin, J. Sann, O. Guillon, F. Tietz, D. Fattakhova-Rohlfing, Survey of Zirconium-Containing NaSICON-type Solid-State Li^+ Ion Conductors with the Aim of Increasing Reduction Stability by Partial Cation Substitution, Batter. Supercaps, 5 (2022) e202200327 https://doi.org/10.1002/batt.202200327

[41] V. Ramar, S. Kumar, S.R. Sivakkumar, P. Balaya, NASICON-type La^{3+}substituted $LiZr_2(PO_4)_3$ with improved ionic conductivity as solid electrolyte, Electrochim. Acta, 271 (2018) 120-126 https://doi.org/10.1016/j.electacta.2018.03.115

[42] M.A. Subramanian, R. Subramanian, A. Clearfield, Lithium ion conductors in the system $AB(IV)_2(PO_4)_3$ (B = Ti, Zr and Hf), Solid State Ion., 18-19 (1986) 562-569 https://doi.org/10.1016/0167-2738(86)90179-7

[43] H. Aono, E. Sugimoto, Y. Sadaoka, N. Imanaka, G.-y. Adachi, Ionic conductivity and sinterability of lithium titanium phosphate system, Solid State Ion., 40-41 (1990) 38-42 https://doi.org/10.1016/0167-2738(90)90282-V

[44] X. Xu, Z. Wen, X. Wu, X. Yang, Z. Gu, Lithium Ion-Conducting Glass–Ceramics of $Li_{1.5}Al_{0.5}Ge_{1.5}(PO_4)_3$–$xLi_2O$ (x=0.0–0.20) with Good Electrical and Electrochemical Properties, J. Am. Ceram. Soc., 90 (2007) 2802-2806 https://doi.org/10.1111/j.1551-2916.2007.01827.x

[45] H. Xie, J.B. Goodenough, Y. Li, $Li_{1.2}Zr_{1.9}Ca_{0.1}(PO_4)_3$, a room-temperature Li-ion solid electrolyte, J. Power Sources, 196 (2011) 7760-7762 https://doi.org/10.1016/j.jpowsour.2011.05.002

[46] Q. Zhou, B. Xu, P.-H. Chien, Y. Li, B. Huang, N. Wu, H. Xu, N.S. Grundish, Y.-Y. Hu, J.B. Goodenough, NASICON $Li_{1.2}Mg_{0.1}Zr_{1.9}(PO_4)_3$ Solid Electrolyte for an All-Solid-State Li-Metal Battery, Small Methods, 4 (2020) 2000764 https://doi.org/10.1002/smtd.202000764

[47] G.G. Amatucci, A. Safari, F.K. Shokoohi, B.J. Wilkens, Lithium scandium phosphate-based electrolytes for solid state lithium rechargeable microbatteries, Solid State Ion., 60 (1993) 357-365 https://doi.org/10.1016/0167-2738(93)90015-U

[48] A. Coelho, TOPAS and TOPAS-Academic: an optimization program integrating computer algebra and crystallographic objects written in C++, J. Appl. Crystallogr., 51 (2018) 210-218 https://doi.org/10.1107/S1600576718000183

[49] Y. Noda, K. Nakano, M. Otake, R. Kobayashi, M. Kotobuki, L. Lu, M. Nakayama, Research Update: Ca doping effect on the Li-ion conductivity in NASICON-type solid electrolyte $LiZr_2(PO_4)_3$: A first-principles molecular dynamics study, APL Mater., 6 (2018) 060702 https://doi.org/10.1063/1.5033460

[50] Y. Yang, W. Chen, X. Lu, Coordination Li diffusion chemistry in NASICON $Li_{1.5}Al_{0.5}Ge_{1.5}(PO_4)_3$ solid electrolyte, Solid State Ion., 381 (2022) 115947 https://doi.org/10.1016/j.ssi.2022.115947

[51] H. Chen, L.L. Wong, S. Adams, SoftBV - a software tool for screening the materials genome of inorganic fast ion conductors, Acta. Crystallogr. B., 75 (2019) 18-33 https://doi.org/10.1107/S2052520618015718

[52] H. Chen, S. Adams, Bond softness sensitive bond-valence parameters for crystal structure plausibility tests, IUCrJ, 4 (2017) 614-625 https://doi.org/10.1107/S2052252517010211

[53] L.L. Wong, K.C. Phuah, R. Dai, H. Chen, W.S. Chew, S. Adams, Bond Valence Pathway Analyzer—An Automatic Rapid Screening Tool for Fast Ion Conductors within softBV, Chem. Mater., 33 (2021) 625-641 https://doi.org/10.1021/acs.chemmater.0c03893

[54] K. Momma, F. Izumi, VESTA: a three-dimensional visualization system for electronic and structural analysis, J. Appl. Crystallogr., 41 (2008) 653-658 https://doi.org/10.1107/S0021889808012016

[55] V. Aravindan, P. Vickraman, K. Krishnaraj, Lithium difluoro(oxalate)borate-based novel nanocomposite polymer electrolytes for lithium ion batteries, Polym. Int., 57 (2008) 932-938 https://doi.org/10.1002/pi.2430

[56] J.-K. Kim, L. Niedzicki, J. Scheers, C.-R. Shin, D.-H. Lim, W. Wieczorek, P. Johansson, J.-H. Ahn, A. Matic, P. Jacobsson, Characterization of N-butyl-N-methyl-pyrrolidinium bis(trifluoromethanesulfonyl)imide-based polymer electrolytes for high safety lithium batteries, J. Power Sources, 224 (2013) 93-98 https://doi.org/10.1016/j.jpowsour.2012.09.029

[57] M. Herstedt, M. Smirnov, P. Johansson, M. Chami, J. Grondin, L. Servant, J.C. Lassègues, Spectroscopic characterization of the conformational states of the bis(trifluoromethanesulfonyl)imide anion ($TFSI^-$), J. Raman Spectrosc., 36 (2005) 762-770 https://doi.org/10.1002/jrs.1347

[58] L.M. McGrath, J. Jones, E. Carey, J.F. Rohan, Ionic Liquid Based Polymer Gel Electrolytes for Use with Germanium Thin Film Anodes in Lithium Ion Batteries, ChemistryOpen, 8 (2019) 1429-1436 https://doi.org/10.1002/open.201900313

[59] F. Croce, L. Persi, B. Scrosati, F. Serraino-Fiory, E. Plichta, M.A. Hendrickson, Role of the ceramic fillers in enhancing the transport properties of composite polymer electrolytes, Electrochim. Acta, 46 (2001) 2457 https://doi.org/10.1016/S0013-4686(01)00458-3

[60] D. Callegari, S. Bonizzoni, V. Berbenni, E. Quartarone, P. Mustarelli, Is It Possible to Obtain Solvent-Free, Li^+-Conducting Solid Electrolytes Based on Pure PVdF? Comment on "Self-Suppression of Lithium Dendrite in All-Solid-State Lithium Metal Batteries with Poly(vinylidene difluoride)-Based Solid Electrolytes", Adv. Mater., 32 (2020) 1907375 https://doi.org/10.1002/adma.201907375

[61] X. Zhang, S. Wang, C. Xue, C. Xin, Y. Lin, Y. Shen, L. Li, C.-W. Nan, Self-Suppression of Lithium Dendrite in All-Solid-State Lithium Metal Batteries with Poly(vinylidene difluoride)-Based Solid Electrolytes, Adv. Mater., 31 (2019) 1806082 https://doi.org/10.1002/adma.201806082

[62] X. Zhang, S. Wang, C. Xue, C. Xin, Y. Lin, Y. Shen, L. Li, C.-W. Nan, Response to Comment on "Self-Suppression of Lithium Dendrite in All-Solid-State Lithium Metal Batteries with Poly(vinylidene difluoride)-Based Solid Electrolytes", Adv. Mater., 32 (2020) 2000026 https://doi.org/10.1002/adma.202000026

[63] Z. Li, H.-M. Huang, J.-K. Zhu, J.-F. Wu, H. Yang, L. Wei, X. Guo, Ionic Conduction in Composite Polymer Electrolytes: Case of PEO:Ga-LLZO Composites, ACS Appl. Mater. Interfaces, 11 (2019) 784-791 https://doi.org/10.1021/acsami.8b17279

[64] W. Fredriksson, K. Edström, XPS study of duplex stainless steel as a possible current collector in a Li-ion battery, Electrochim. Acta, 79 (2012) 82-94 https://doi.org/10.1016/j.electacta.2012.06.057

[65] M. Rosso, T. Gobron, C. Brissot, J.N. Chazalviel, S. Lascaud, Onset of dendritic growth in lithium/polymer cells, J. Power Sources, 97-98 (2001) 804-806 https://doi.org/10.1016/S0378-7753(01)00734-0

[66] J.N. Chazalviel, Electrochemical aspects of the generation of ramified metallic electrodeposits, Physical Review A, 42 (1990) 7355-7367 https://doi.org/10.1103/PhysRevA.42.7355

[67] J. Evans, C.A. Vincent, P.G. Bruce, Electrochemical measurement of transference numbers in polymer electrolytes, Polymer, 28 (1987) 2324 https://doi.org/10.1016/0032-3861(87)90394-6

[68] K.-H. Chen, K.N. Wood, E. Kazyak, W.S. LePage, A.L. Davis, A.J. Sanchez, N.P. Dasgupta, Dead lithium: mass transport effects on voltage, capacity, and failure of lithium metal anodes, J. Mater. Chem. A, 5 (2017) 11671-11681 https://doi.org/10.1039/C7TA00371D

[69] S. Xia, J. Lopez, C. Liang, Z. Zhang, Z. Bao, Y. Cui, W. Liu, High-Rate and Large-Capacity Lithium Metal Anode Enabled by Volume Conformal and Self-Healable Composite Polymer Electrolyte, Adv. Sci., 6 (2019) 1802353 https://doi.org/10.1002/advs.201802353

[70] Y.L. Liao, J.K. Hu, Z.H. Fu, C.Z. Zhao, Y. Lu, S. Li, S.J. Yang, S. Sun, X.L. Wang, J. Liu, J.Q. Huang, H. Yuan, Integrated interface configuration by in-situ interface chemistry enabling uniform lithium deposition in all-solid-state lithium metal batteries, J. Energy Chem., 80 (2023) 458-465 https://doi.org/10.1016/j.jechem.2023.02.012

[71] X.R. Chen, C. Yan, J.F. Ding, H.J. Peng, Q. Zhang, New insights into “dead lithium” during stripping in lithium metal batteries, J. Energy Chem., 62 (2021) 289-294 https://doi.org/10.1016/j.jechem.2021.03.048

[72] M. Zhou, Y. Liao, L. Li, R. Xiong, G. Shen, Y. Chen, T. Huang, M. Li, H. Zhou, Y. Zhang, Unraveling the heterogeneity of solid electrolyte interphase kinetically affecting lithium electrodeposition on lithium metal anode, J. Energy Chem., 85 (2023) 181-190 https://doi.org/10.1016/j.jechem.2023.06.008

[Supplementary Information]

Enhancing Room Temperature Performance of Solid-State Lithium Cell via a Facile Solid Electrolyte-Cathode Interface Design

Asish Kumar Das[a], Manish Badole[a], Hari Narayanan Vasavan[a], Samriddhi Saxena[a], Pratiksha Gami[a], Sonia Deswal[b], Pradeep Kumar[b], Sunil Kumar [a,c,*]

[a]Department of Metallurgical Engineering and Materials Science, Indian Institute of Technology Indore, Simrol, 453552, India

[b]School of Physical Sciences, Indian Institute of Technology Mandi, Himachal Pradesh, 175005, India

[c]Center for Electric Vehicle and Intelligent Transport Systems, Indian Institute of Technology Indore, Simrol, 453552, India

*Corresponding author E-mail: sunil@iiti.ac.in

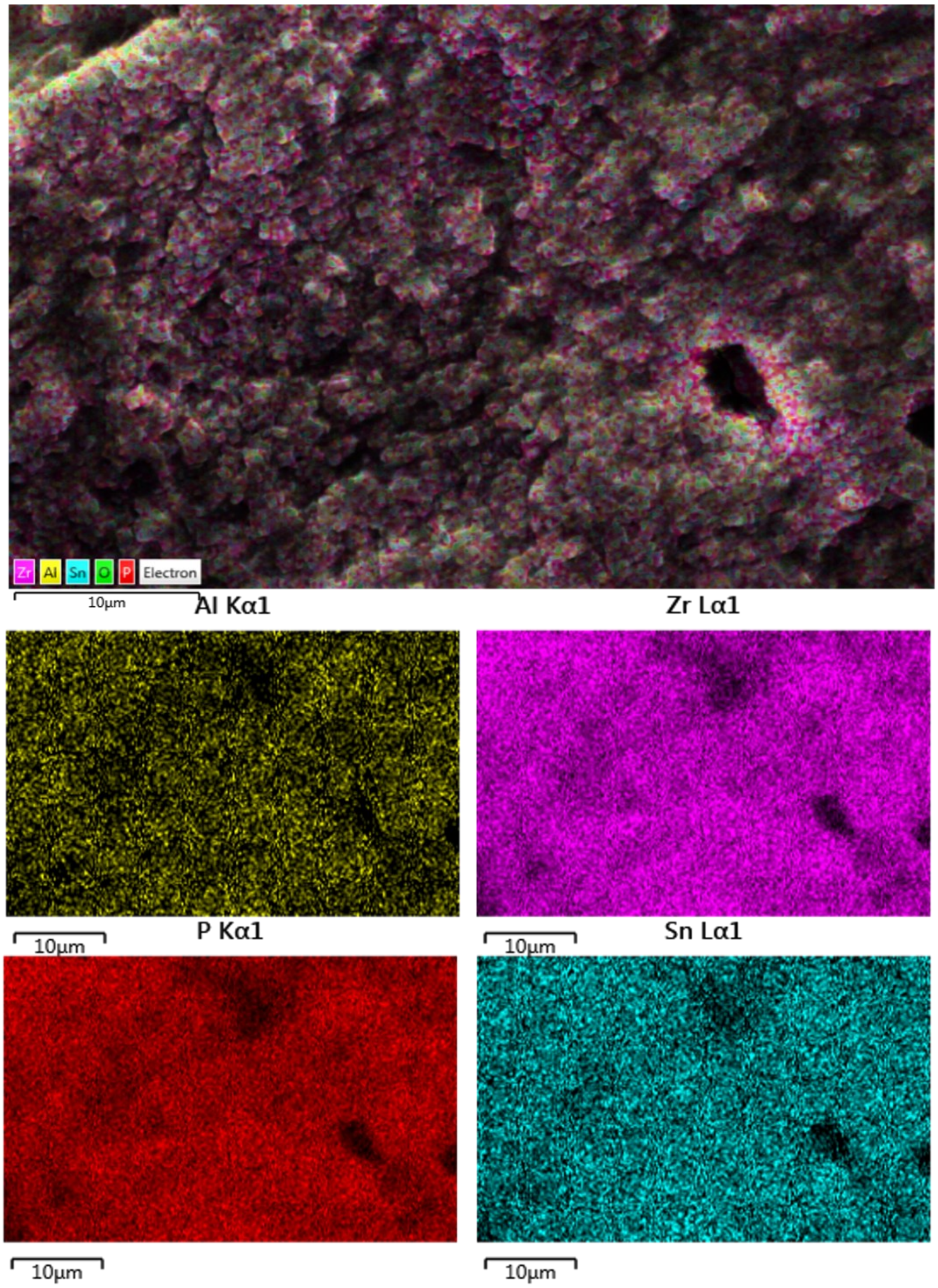

Figure S1: EDS mapping of LSZAP.

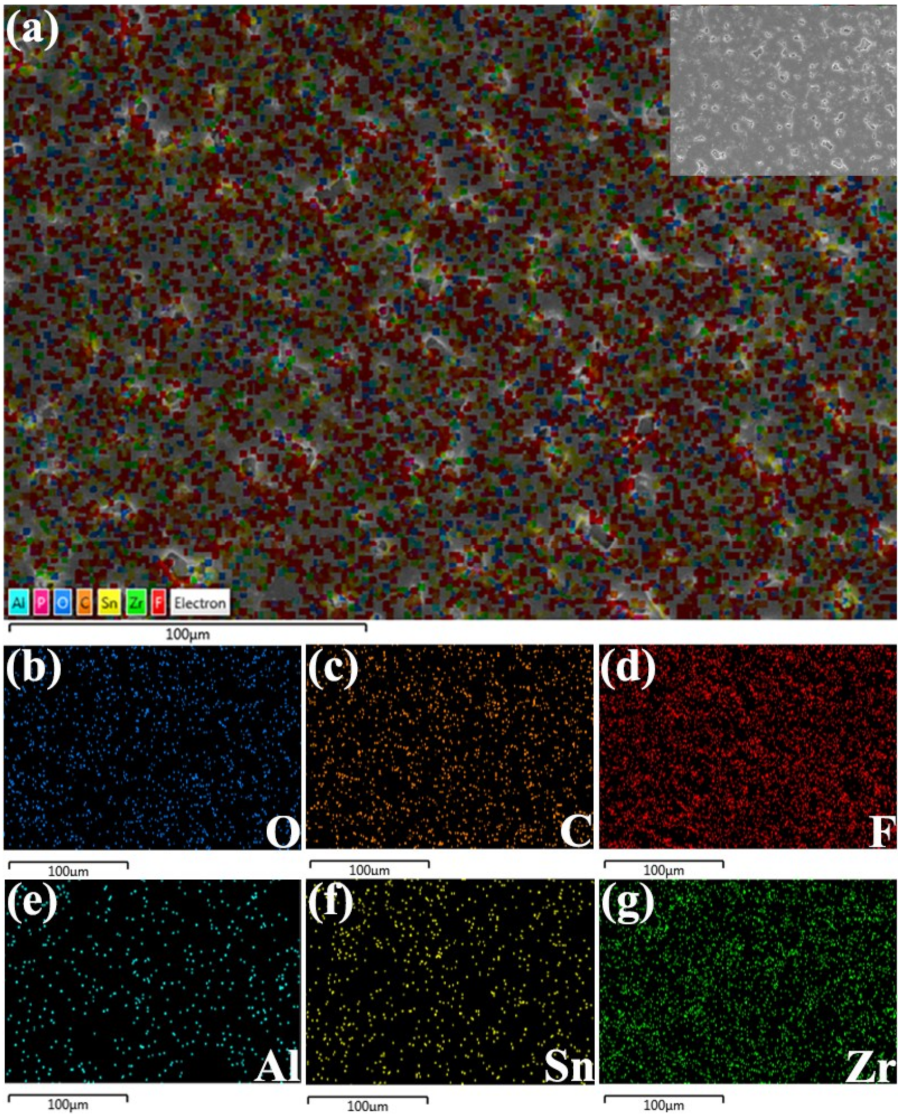

Figure S2: SEM image and EDS mapping of CPSE15.

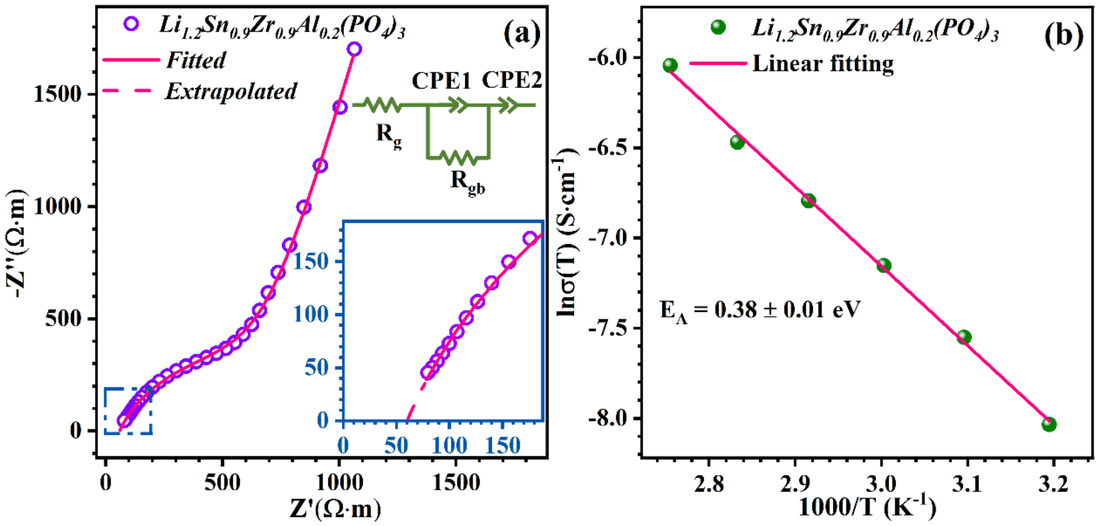

Figure S3: (a) Room temperature Nyquist plot of $Li_{1.2}Sn_{0.9}Zr_{0.9}Al_{0.2}(PO_4)_3$ (insets display the equivalent circuit used for fitting the impedance data and zoomed view at high frequency) and (b) Linear fitting using Arrhenius equation for $Li_{1.2}Sn_{0.9}Zr_{0.9}Al_{0.2}(PO_4)_3$ sample.

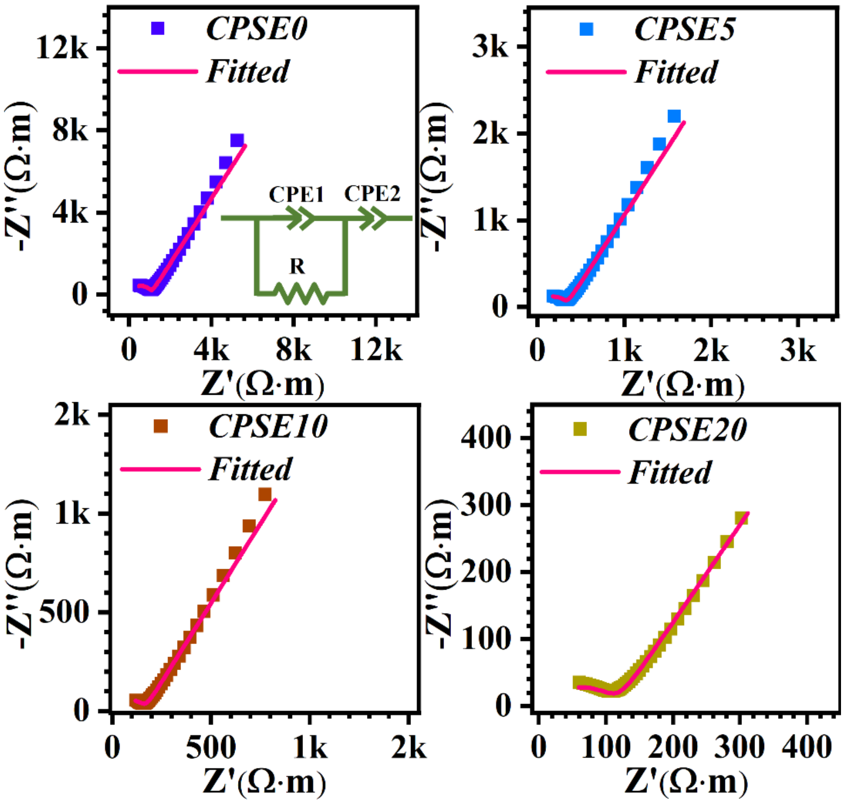

Figure S4: Room temperature Nyquist plots of CPSEx (x = 0, 5, 10, and 20) and inset displays the equivalent circuit used for fitting the impedance data.

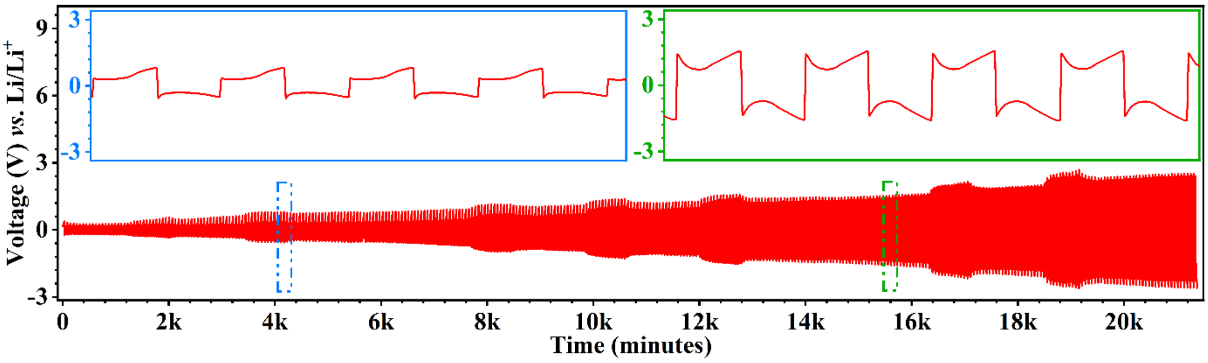

Figure S5: Galvanostatic charge-discharge profile of symmetric Li|CPSE0|Li cell at a current density of 0.1 mA cm^{-2}.

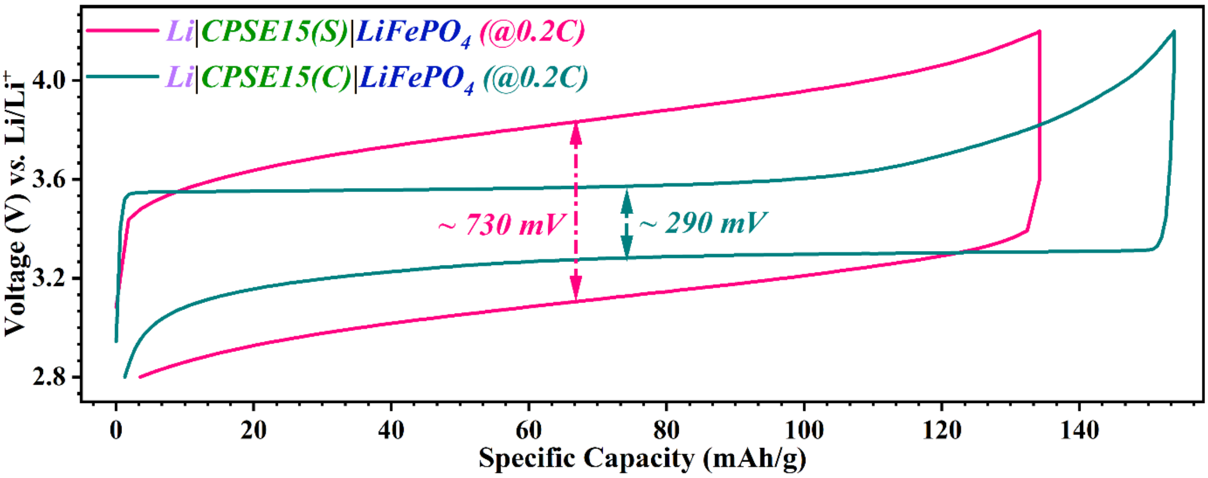

Figure S6: GCD profile of Li|CPSE15(C)|LiFePO$_4$ and Li|CPSE15(S)|LiFePO$_4$ cells at 0.2 C.

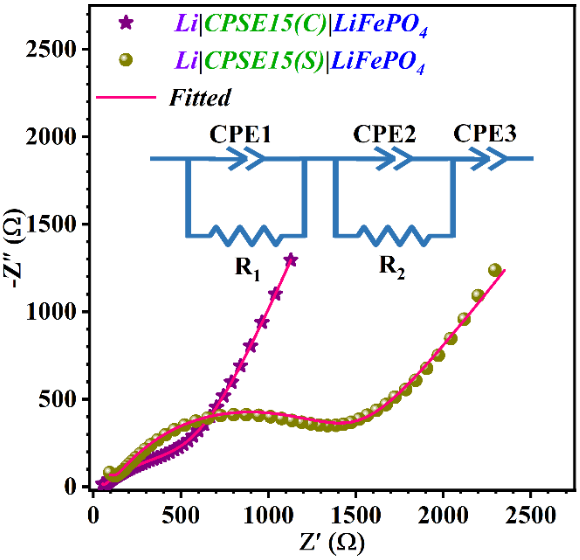

Figure S7: Room temperature Nyquist plots of Li|CPSE15(C)|LiFePO$_4$ and Li|CPSE15(S)|LiFePO$_4$ cells and the inset presents the equivalent circuit used for fitting the impedance data.

Table S3: Parameters obtained from fitting Nyquist plots of Li|CPSE15(C)|LiFePO$_4$ and Li|CPSE15(S)|LiFePO$_4$ using eissa1 software with the equivalent circuit shown in Fig. S5 inset.

Fitted Parameters\ Sample	**Li|CPSE15(C)|LiFePO$_4$ cell**	**Li|CPSE15(S)|LiFePO$_4$ cell**
R1 (Ω)	50	101
R2 (Ω)	631	1307
P1 (F s^{n-1})	7.78E-10	9.60E-09
P2 (F s^{n-1})	9.78E-05	4.91E-06
P3 (F s^{n-1})	1.86E-04	2.28E-04
n1	0.75	1
n2	0.46	0.67
n3	1	0.57

Table S2: Comparison of the performance of our composite solid electrolyte with other P(VDF-HFP) based composite solid electrolytes.

Ceramic Filler	**Conductivity (S cm^{-1})**	**Transference number**	**Temperature (°C)**	**Ref.**
$Li_{6.28}Al_{0.24}La_3Zr_2O_{12}$ and hexagonal-BN	1.1×10^{-4}	0.63	25	[73]
$Li_{6.5}La_3Zr_{1.5}Ta_{0.5}O_{12}$	8.8×10^{-5}	0.47	RT	[74]
Ga-Doped-LLZO ($Li_7La_3Zr_2O_{12}$)	1.05×10^{-4}	0.52 (60 °C)	35	[75]
LATP/graphitic-C_3N_4	2.55×10^{-5}	0.647	25	[76]
$Li_{6.25}Ga_{0.25}La_3Zr_2O_{12}$	1.1×10^{-4}	0.87	RT	[77]
LLZO	6.2×10^{-5}	0.376	25	[78]
$Li_{6.4}La_3Zr_{1.4}Ta_{0.6}O_{12}$	6.86×10^{-5}	0.48	30	[79]
$Li_{6.4}La_{3.0}Zr_{1.4}Ta_{0.6}O_{12}$	5.5×10^{-5}	0.21	30	[80]
$Li_{1.2}Sn_{0.9}Zr_{0.9}(PO_4)_3$	1.1×10^{-4}	0.60	25	**This work**

References:

[1] J.B. Goodenough, K.-S. Park, The Li-Ion Rechargeable Battery: A Perspective, J. Am. Chem. Soc., 135 (2013) 1167 https://doi.org/10.1021/ja3091438

[2] B. Diouf, R. Pode, Potential of lithium-ion batteries in renewable energy, Renew. Energ., 76 (2015) 375 https://doi.org/10.1016/j.renene.2014.11.058

[3] E.C. Evarts, Lithium batteries: To the limits of lithium, Nature, 526 (2015) S93 https://doi.org/10.1038/526S93a

[4] H.N. Vasavan, M. Badole, S. Saxena, A.K. Das, S. Deswal, P. Kumar, S. Kumar, Excellent Structural Stability-Driven Cyclability in P2-Type Ti-Based Cathode for Na-Ion Batteries, ACS Appl. Energy Mater., 6 (2023) 2440-2447 https://doi.org/10.1021/acsaem.2c03750

[5] S. Saxena, H.N. Vasavan, M. Badole, A.K. Das, S. Deswal, P. Kumar, S. Kumar, Tailored P2/O3 phase-dependent electrochemical behavior of Mn-based cathode for sodium-ion batteries, J. Energy Storage, 64 (2023) https://doi.org/10.1016/j.est.2023.107242

[6] S. Megahed, W. Ebner, Lithium-ion battery for electronic applications, J. Power Sources, 54 (1995) 155 https://doi.org/10.1016/0378-7753(94)02059-C

[7] R. Song, J. Yao, R. Xu, Z. Li, X. Yan, C. Yu, Z. Huang, L. Zhang, Metastable Decomposition Realizing Dendrite-Free Solid-State Li Metal Batteries, Adv. Energy Mater., 13 (2023) 2203631 https://doi.org/10.1002/aenm.202203631

[8] N. Nitta, F. Wu, J.T. Lee, G. Yushin, Li-ion battery materials: present and future, Mater. Today, 18 (2015) 252 https://doi.org/10.1016/j.mattod.2014.10.040

[9] L. Li, J. Yao, R. Xu, Q. Lin, X. Yan, C. Yu, L. Zhang, Highly stable and encapsulation-microstructural cathode derived by self-pressurization behavior in Na-halides-based all-solid-state batteries, Energy Storage Mater., 63 (2023) 103016 https://doi.org/10.1016/j.ensm.2023.103016

[10] S. Chen, C. Yu, C. Wei, Z. Jiang, Z. Zhang, L. Peng, S. Cheng, J. Xie, Unraveling Electrochemical Stability and Reversible Redox of Y-Doped Li_2ZrCl_6 Solid Electrolytes, Energy Mater. Adv., 4 (2023) 0019 https://doi.org/10.34133/energymatadv.0019

[11] D. Zeng, J. Yao, L. Zhang, R. Xu, S. Wang, X. Yan, C. Yu, L. Wang, Promoting favorable interfacial properties in lithium-based batteries using chlorine-rich sulfide inorganic solid-state electrolytes, Nat. Commun., 13 (2022) 1909 https://doi.org/10.1038/s41467-022-29596-8

[12] C. Li, X. Zhang, Z. Yang, H. Lv, T. Song, S. Lu, Y. Zhang, T. Yang, F. Xu, F. Wu, D. Mu, Stable cycling of $LiNi_{0.9}Co_{0.05}Mn_{0.05}O_2$/lithium metal batteries enabled by synergistic tuning the surface stability of cathode/anode, J. Energy Chem., 87 (2023) 342-350 https://doi.org/10.1016/j.jechem.2023.08.033

[13] R. Guo, W. Han, The effects of electrolytes, electrolyte/electrode interphase, and binders on lithium-ion batteries at low temperature, Mater. Today Sustain., 19 (2022) 100187 https://doi.org/10.1016/j.mtsust.2022.100187

[14] T. Kim, Voltage-dependent formation of cathode–electrolyte interphase with independent metallic layer in $LiNi_{0.8}Mn_{0.1}Co_{0.1}O_2$ cathode for high-energy density lithium-ion batteries, Mater. Today Sustain., 21 (2023) 100326 https://doi.org/10.1016/j.mtsust.2023.100326

[15] S. Jian, Y. Cao, W. Feng, G. Yin, Y. Zhao, Y. Lai, T. Zhang, X. Ling, H. Wu, H. Bi, Y. Dong, Recent progress in solid polymer electrolytes with various dimensional fillers: a review, Mater. Today Sustain., 20 (2022) 100224 https://doi.org/10.1016/j.mtsust.2022.100224

[16] X. Zhao, P. Xiang, J. Wu, Z. Liu, L. Shen, G. Liu, Z. Tian, L. Chen, X. Yao, Toluene Tolerated $Li_{9.88}GeP_{1.96}Sb_{0.04}S_{11.88}Cl_{0.12}$ Solid Electrolyte toward Ultrathin Membranes for All-Solid-State Lithium Batteries, Nano Lett., 23 (2023) 227-234 https://doi.org/10.1021/acs.nanolett.2c04140

[17] P. Yu, N. Ahmad, J. Yang, C. Zeng, X. Liang, W. Huang, M. Ni, P. Mao, W. Yang, Dual-doping for enhancing chemical stability of functional anionic units in sulfide for high-performance all-solid-state lithium batteries, J. Energy Chem., 86 (2023) 382-390 https://doi.org/10.1016/j.jechem.2023.07.038

[18] X. Yu, A. Manthiram, A review of composite polymer-ceramic electrolytes for lithium batteries, Energy Storage Mater., 34 (2021) 282-300 https://doi.org/10.1016/j.ensm.2020.10.006

[19] H. Jeon, H.A. Hoang, D. Kim, Flexible PVA/BMIMOTf/LLZTO composite electrolyte with liquid-comparable ionic conductivity for solid-state lithium metal battery, J. Energy Chem., 74 (2022) 128-139 https://doi.org/10.1016/j.jechem.2022.07.014

[20] T. Huang, W. Xiong, X. Ye, Z. Huang, Y. Feng, J. Liang, S. Ye, J. Piao, X. Wang, Y. Li, X. Ren, C. Chen, S. Huang, X. Ouyang, Q. Zhang, J. Liu, A cerium-doped NASICON chemically coupled poly(vinylidene fluoride-hexafluoropropylene)-based polymer electrolyte for high-rate and high-voltage quasi-solid-state lithium metal batteries, J. Energy Chem., 73 (2022) 311-321 https://doi.org/10.1016/j.jechem.2022.06.030

[21] D. Kim, C. Bak, N. Kim, J. Park, M.J. Lee, D.O. Shin, Y.G. Lee, Y.M. Lee, Surface-patterned graphite electrode with hybrid polymer/garnet electrolyte for all-solid-state batteries, Mater. Today Sustain., 22 (2023) 100338 https://doi.org/10.1016/j.mtsust.2023.100338

[22] Z. Zhang, X. Wang, X. Li, J. Zhao, G. Liu, W. Yu, X. Dong, J. Wang, Review on composite solid electrolytes for solid-state lithium-ion batteries, Mater. Today Sustain., 21 (2023) 100316 https://doi.org/10.1016/j.mtsust.2023.100316

[23] X. Zhang, T. Liu, S. Zhang, X. Huang, B. Xu, Y. Lin, B. Xu, L. Li, C.-W. Nan, Y. Shen, Synergistic Coupling between $Li_{6.75}La_3Zr_{1.75}Ta_{0.25}O_{12}$ and Poly(vinylidene fluoride) Induces High Ionic Conductivity, Mechanical Strength, and Thermal Stability of Solid Composite Electrolytes, J. Am. Chem. Soc., 139 (2017) 13779-13785 https://doi.org/10.1021/jacs.7b06364

[24] S. Choudhary, R.J. Sengwa, Effects of different inorganic nanoparticles on the structural, dielectric and ion transportation properties of polymers blend based nanocomposite solid polymer electrolytes, Electrochim. Acta, 247 (2017) 924-941 https://doi.org/10.1016/j.electacta.2017.07.051

[25] B. Luo, W. Wang, Q. Wang, W. Ji, G. Yu, Z. Liu, Z. Zhao, X. Wang, S. Wang, J. Zhang, Facilitating ionic conductivity and interfacial stability via oxygen vacancies-enriched TiO_2 microrods for composite polymer electrolytes, Chem. Eng. J., 460 (2023) 141329 https://doi.org/10.1016/j.cej.2023.141329

[26] K. Khan, B. Fu, H. Xin, B.A. Beshiwork, M.B. Hanif, J. Wu, Z. Fang, J. Yang, T. Li, C. Chen, M. Motola, Z. Xu, M. Wu, Composite polymer electrolyte incorporating WO_3 nanofillers with enhanced performance for dendrite-free solid-state lithium battery, Ceram. Int., 49 (2023) 4473-4481 https://doi.org/10.1016/j.ceramint.2022.09.333

[27] T. Yang, J. Zheng, Q. Cheng, Y.-Y. Hu, C.K. Chan, Composite Polymer Electrolytes with $Li_7La_3Zr_2O_{12}$ Garnet-Type Nanowires as Ceramic Fillers: Mechanism of Conductivity Enhancement and Role of Doping and Morphology, ACS Appl. Mater. Interfaces, 9 (2017) 21773-21780 https://doi.org/10.1021/acsami.7b03806

[28] P. Sivaraj, K.P. Abhilash, B. Nalini, P. Perumal, P.C. Selvin, Free-standing, high Li-ion conducting hybrid PAN/PVdF/$LiClO_4$/$Li_{0.5}La_{0.5}TiO_3$ nanocomposite solid polymer electrolytes for all-solid-state batteries, J. Solid State Electrochem., 25 (2021) 905-917 https://doi.org/10.1007/s10008-020-04858-x

[29] B.-J. Sung, P.N. Didwal, R. Verma, A.-G. Nguyen, D.R. Chang, C.-J. Park, Composite solid electrolyte comprising poly(propylene carbonate) and $Li_{1.5}Al_{0.5}Ge_{1.5}(PO_4)_3$ for long-life all-solid-state Li-ion batteries, Electrochim. Acta, 392 (2021) 139007 https://doi.org/10.1016/j.electacta.2021.139007

[30] S. Li, J. Lu, Z. Geng, Y. Chen, X. Yu, M. He, H. Li, Solid Polymer Electrolyte Reinforced with a $Li_{1.3}Al_{0.3}Ti_{1.7}(PO_4)_3$-Coated Separator for All-Solid-State Lithium Batteries, ACS Appl. Mater. Interfaces, 14 (2022) 1195-1202 https://doi.org/10.1021/acsami.1c21804

[31] X. Lu, Y. Wang, X. Xu, B. Yan, T. Wu, L. Lu, Polymer-Based Solid-State Electrolytes for High-Energy-Density Lithium-Ion Batteries – Review, Adv. Energy Mater., 13 (2023) 2301746 https://doi.org/10.1002/aenm.202301746

[32] L. Liu, D. Zhang, T. Yang, W. Hu, X. Meng, J. Mo, W. Hou, Q. Fan, K. Liu, B. Jiang, L. Chu, M. Li, Flexible ion-conducting membranes with 3D continuous nanohybrid networks for high-performance solid-state metallic lithium batteries, J. Energy Chem., 75 (2022) 360-368 https://doi.org/10.1016/j.jechem.2022.08.036

[33] L. Zhai, K. Yang, F. Jiang, W. Liu, Z. Yan, J. Sun, High-performance solid-state lithium metal batteries achieved by interface modification, J. Energy Chem., 79 (2023) 357-364 https://doi.org/10.1016/j.jechem.2023.01.022

[34] H. Yan, J. Yao, Z. Ye, Q. Lin, Z. Zhang, S. Li, D. Song, Z. Wang, C. Yu, L. Zhang, Al-F co-doping towards enhanced electrolyte-electrodes interface properties for halide and sulfide solid electrolytes, Chin. Chem. Lett., (2024) 109568 https://doi.org/10.1016/j.cclet.2024.109568

[35] T. Pareek, B. Singh, S. Dwivedi, A.K. Yadav, Anita, S. Sen, P. Kumar, S. Kumar, Ionic conduction and vibrational characteristics of Al^{3+} modified monoclinic $LiZr_2(PO_4)_3$, Electrochim. Acta, 263 (2018) 533-543 https://doi.org/10.1016/j.electacta.2018.01.087

[36] S. Kumar, P. Balaya, Improved ionic conductivity in NASICON-type Sr^{2+} doped $LiZr_2(PO_4)_3$, Solid State Ion., 296 (2016) 1-6 https://doi.org/10.1016/j.ssi.2016.08.012

[37] S.A. Ahmed, T. Pareek, S. Dwivedi, M. Badole, S. Kumar, $LiSn_2(PO_4)_3$-based polymer-in-ceramic composite electrolyte with high ionic conductivity for all-solid-state lithium batteries, J. Solid State Electrochem., 24 (2020) 2407-2417 https://doi.org/10.1007/s10008-020-04783-z

[38] T. Pareek, S. Dwivedi, B. Singh, D. Kumar, P. Kumar, S. Kumar, $LiSnZr(PO_4)_3$: NASICON-type solid electrolyte with excellent room temperature Li^+ conductivity, J. Alloys Compd., 777 (2019) 602-611 https://doi.org/10.1016/j.jallcom.2018.10.384

[39] A.K. Das, M. Badole, H.N. Vasavan, S. Saxena, P. Gami, S. Kumar, Highly conductive ceramic-in-polymer composite electrolyte enabling superior electrochemical performance for all-solid-state lithium batteries, Ceram. Int., 49 (2023) 29719-29728 https://doi.org/10.1016/j.ceramint.2023.06.214

[40] A. Loutati, P. Odenwald, B. Aktekin, J. Sann, O. Guillon, F. Tietz, D. Fattakhova-Rohlfing, Survey of Zirconium-Containing NaSICON-type Solid-State Li^+ Ion Conductors with the Aim of Increasing Reduction Stability by Partial Cation Substitution, Batter. Supercaps, 5 (2022) e202200327 https://doi.org/10.1002/batt.202200327

[41] V. Ramar, S. Kumar, S.R. Sivakkumar, P. Balaya, NASICON-type La^{3+}substituted $LiZr_2(PO_4)_3$ with improved ionic conductivity as solid electrolyte, Electrochim. Acta, 271 (2018) 120-126 https://doi.org/10.1016/j.electacta.2018.03.115

[42] M.A. Subramanian, R. Subramanian, A. Clearfield, Lithium ion conductors in the system $AB(IV)_2(PO_4)_3$ (B = Ti, Zr and Hf), Solid State Ion., 18-19 (1986) 562-569 https://doi.org/10.1016/0167-2738(86)90179-7

[43] H. Aono, E. Sugimoto, Y. Sadaoka, N. Imanaka, G.-y. Adachi, Ionic conductivity and sinterability of lithium titanium phosphate system, Solid State Ion., 40-41 (1990) 38-42 https://doi.org/10.1016/0167-2738(90)90282-V

[44] X. Xu, Z. Wen, X. Wu, X. Yang, Z. Gu, Lithium Ion-Conducting Glass–Ceramics of $Li_{1.5}Al_{0.5}Ge_{1.5}(PO_4)_3$–$xLi_2O$ (x=0.0–0.20) with Good Electrical and Electrochemical Properties, J. Am. Ceram. Soc., 90 (2007) 2802-2806 https://doi.org/10.1111/j.1551-2916.2007.01827.x

[45] H. Xie, J.B. Goodenough, Y. Li, $Li_{1.2}Zr_{1.9}Ca_{0.1}(PO_4)_3$, a room-temperature Li-ion solid electrolyte, J. Power Sources, 196 (2011) 7760-7762 https://doi.org/10.1016/j.jpowsour.2011.05.002

[46] Q. Zhou, B. Xu, P.-H. Chien, Y. Li, B. Huang, N. Wu, H. Xu, N.S. Grundish, Y.-Y. Hu, J.B. Goodenough, NASICON $Li_{1.2}Mg_{0.1}Zr_{1.9}(PO_4)_3$ Solid Electrolyte for an All-Solid-State Li-Metal Battery, Small Methods, 4 (2020) 2000764 https://doi.org/10.1002/smtd.202000764

[47] G.G. Amatucci, A. Safari, F.K. Shokoohi, B.J. Wilkens, Lithium scandium phosphate-based electrolytes for solid state lithium rechargeable microbatteries, Solid State Ion., 60 (1993) 357-365 https://doi.org/10.1016/0167-2738(93)90015-U

[48] A. Coelho, TOPAS and TOPAS-Academic: an optimization program integrating computer algebra and crystallographic objects written in C++, J. Appl. Crystallogr., 51 (2018) 210-218 https://doi.org/10.1107/S1600576718000183

[49] Y. Noda, K. Nakano, M. Otake, R. Kobayashi, M. Kotobuki, L. Lu, M. Nakayama, Research Update: Ca doping effect on the Li-ion conductivity in NASICON-type solid electrolyte $LiZr_2(PO_4)_3$: A first-principles molecular dynamics study, APL Mater., 6 (2018) 060702 https://doi.org/10.1063/1.5033460

[50] Y. Yang, W. Chen, X. Lu, Coordination Li diffusion chemistry in NASICON $Li_{1.5}Al_{0.5}Ge_{1.5}(PO_4)_3$ solid electrolyte, Solid State Ion., 381 (2022) 115947 https://doi.org/10.1016/j.ssi.2022.115947

[51] H. Chen, L.L. Wong, S. Adams, SoftBV - a software tool for screening the materials genome of inorganic fast ion conductors, Acta. Crystallogr. B., 75 (2019) 18-33 https://doi.org/10.1107/S2052520618015718

[52] H. Chen, S. Adams, Bond softness sensitive bond-valence parameters for crystal structure plausibility tests, IUCrJ, 4 (2017) 614-625 https://doi.org/10.1107/S2052252517010211

[53] L.L. Wong, K.C. Phuah, R. Dai, H. Chen, W.S. Chew, S. Adams, Bond Valence Pathway Analyzer—An Automatic Rapid Screening Tool for Fast Ion Conductors within softBV, Chem. Mater., 33 (2021) 625-641 https://doi.org/10.1021/acs.chemmater.0c03893

[54] K. Momma, F. Izumi, VESTA: a three-dimensional visualization system for electronic and structural analysis, J. Appl. Crystallogr., 41 (2008) 653-658 https://doi.org/10.1107/S0021889808012016

[55] V. Aravindan, P. Vickraman, K. Krishnaraj, Lithium difluoro(oxalate)borate-based novel nanocomposite polymer electrolytes for lithium ion batteries, Polym. Int., 57 (2008) 932-938 https://doi.org/10.1002/pi.2430

[56] J.-K. Kim, L. Niedzicki, J. Scheers, C.-R. Shin, D.-H. Lim, W. Wieczorek, P. Johansson, J.-H. Ahn, A. Matic, P. Jacobsson, Characterization of N-butyl-N-methyl-pyrrolidinium bis(trifluoromethanesulfonyl)imide-based polymer electrolytes for high safety lithium batteries, J. Power Sources, 224 (2013) 93-98 https://doi.org/10.1016/j.jpowsour.2012.09.029

[57] M. Herstedt, M. Smirnov, P. Johansson, M. Chami, J. Grondin, L. Servant, J.C. Lassègues, Spectroscopic characterization of the conformational states of the bis(trifluoromethanesulfonyl)imide anion ($TFSI^-$), J. Raman Spectrosc., 36 (2005) 762-770 https://doi.org/10.1002/jrs.1347

[58] L.M. McGrath, J. Jones, E. Carey, J.F. Rohan, Ionic Liquid Based Polymer Gel Electrolytes for Use with Germanium Thin Film Anodes in Lithium Ion Batteries, ChemistryOpen, 8 (2019) 1429-1436 https://doi.org/10.1002/open.201900313

[59] F. Croce, L. Persi, B. Scrosati, F. Serraino-Fiory, E. Plichta, M.A. Hendrickson, Role of the ceramic fillers in enhancing the transport properties of composite polymer electrolytes, Electrochim. Acta, 46 (2001) 2457 https://doi.org/10.1016/S0013-4686(01)00458-3

[60] D. Callegari, S. Bonizzoni, V. Berbenni, E. Quartarone, P. Mustarelli, Is It Possible to Obtain Solvent-Free, Li^+-Conducting Solid Electrolytes Based on Pure PVdF? Comment on “Self-Suppression of Lithium Dendrite in All-Solid-State Lithium Metal Batteries with

Poly(vinylidene difluoride)-Based Solid Electrolytes", Adv. Mater., 32 (2020) 1907375 https://doi.org/10.1002/adma.201907375

[61] X. Zhang, S. Wang, C. Xue, C. Xin, Y. Lin, Y. Shen, L. Li, C.-W. Nan, Self-Suppression of Lithium Dendrite in All-Solid-State Lithium Metal Batteries with Poly(vinylidene difluoride)-Based Solid Electrolytes, Adv. Mater., 31 (2019) 1806082 https://doi.org/10.1002/adma.201806082

[62] X. Zhang, S. Wang, C. Xue, C. Xin, Y. Lin, Y. Shen, L. Li, C.-W. Nan, Response to Comment on "Self-Suppression of Lithium Dendrite in All-Solid-State Lithium Metal Batteries with Poly(vinylidene difluoride)-Based Solid Electrolytes", Adv. Mater., 32 (2020) 2000026 https://doi.org/10.1002/adma.202000026

[63] Z. Li, H.-M. Huang, J.-K. Zhu, J.-F. Wu, H. Yang, L. Wei, X. Guo, Ionic Conduction in Composite Polymer Electrolytes: Case of PEO:Ga-LLZO Composites, ACS Appl. Mater. Interfaces, 11 (2019) 784-791 https://doi.org/10.1021/acsami.8b17279

[64] W. Fredriksson, K. Edström, XPS study of duplex stainless steel as a possible current collector in a Li-ion battery, Electrochim. Acta, 79 (2012) 82-94 https://doi.org/10.1016/j.electacta.2012.06.057

[65] M. Rosso, T. Gobron, C. Brissot, J.N. Chazalviel, S. Lascaud, Onset of dendritic growth in lithium/polymer cells, J. Power Sources, 97-98 (2001) 804-806 https://doi.org/10.1016/S0378-7753(01)00734-0

[66] J.N. Chazalviel, Electrochemical aspects of the generation of ramified metallic electrodeposits, Physical Review A, 42 (1990) 7355-7367 https://doi.org/10.1103/PhysRevA.42.7355

[67] J. Evans, C.A. Vincent, P.G. Bruce, Electrochemical measurement of transference numbers in polymer electrolytes, Polymer, 28 (1987) 2324 https://doi.org/10.1016/0032-3861(87)90394-6

[68] K.-H. Chen, K.N. Wood, E. Kazyak, W.S. LePage, A.L. Davis, A.J. Sanchez, N.P. Dasgupta, Dead lithium: mass transport effects on voltage, capacity, and failure of lithium metal anodes, J. Mater. Chem. A, 5 (2017) 11671-11681 https://doi.org/10.1039/C7TA00371D

[69] S. Xia, J. Lopez, C. Liang, Z. Zhang, Z. Bao, Y. Cui, W. Liu, High-Rate and Large-Capacity Lithium Metal Anode Enabled by Volume Conformal and Self-Healable Composite Polymer Electrolyte, Adv. Sci., 6 (2019) 1802353 https://doi.org/10.1002/advs.201802353

[70] Y.L. Liao, J.K. Hu, Z.H. Fu, C.Z. Zhao, Y. Lu, S. Li, S.J. Yang, S. Sun, X.L. Wang, J. Liu, J.Q. Huang, H. Yuan, Integrated interface configuration by in-situ interface chemistry enabling uniform lithium deposition in all-solid-state lithium metal batteries, J. Energy Chem., 80 (2023) 458-465 https://doi.org/10.1016/j.jechem.2023.02.012

[71] X.R. Chen, C. Yan, J.F. Ding, H.J. Peng, Q. Zhang, New insights into "dead lithium" during stripping in lithium metal batteries, J. Energy Chem., 62 (2021) 289-294 https://doi.org/10.1016/j.jechem.2021.03.048

[72] M. Zhou, Y. Liao, L. Li, R. Xiong, G. Shen, Y. Chen, T. Huang, M. Li, H. Zhou, Y. Zhang, Unraveling the heterogeneity of solid electrolyte interphase kinetically affecting lithium electrodeposition on lithium metal anode, J. Energy Chem., 85 (2023) 181-190 https://doi.org/10.1016/j.jechem.2023.06.008

[73] J.H. Kim, D.H. Park, J.S. Jang, J.H. Shin, M.C. Kim, S.B. Kim, S.H. Moon, S.N. Lee, K.W. Park, High-performance free-standing hybrid solid electrolyte membrane combined with

Li6.28Al0.24La3Zr2O12 and hexagonal-BN for all-solid-state lithium-based batteries, Chem. Eng. J., 446 (2022) 10.1016/j.cej.2022.137035

[74] J. Lu, Y. Liu, P. Yao, Z. Ding, Q. Tang, J. Wu, Z. Ye, K. Huang, X. Liu, Hybridizing poly(vinylidene fluoride-co-hexafluoropropylene) with Li6.5La3Zr1.5Ta0.5O12 as a lithium-ion electrolyte for solid state lithium metal batteries, Chem. Eng. J., 367 (2019) 230-238 10.1016/j.cej.2019.02.148

[75] J. Huang, Y. Huang, Z. Zhang, H. Gao, C. Li, Li6.7La3Zr1.7Ta0.3O12Reinforced PEO/PVDF-HFP Based Composite Solid Electrolyte for All Solid-State Lithium Metal Battery, Energy Fuels, 34 (2020) 15011-15018 10.1021/acs.energyfuels.0c03124

[76] Q. Zhang, Q. Wang, S. Huang, Y. Jiang, Z. Chen, Preparation and electrochemical study of PVDF-HFP/LATP/g-C3N4 composite polymer electrolyte membrane, Inorg. Chem. Commun., 131 (2021) 10.1016/j.inoche.2021.108793

[77] J. Cai, T. Liu, C. Liu, G. Liu, PVDF-HFP/LiTFSI based composite solid state electrolyte with different micromorphology of Li6.25Ga0.25La3Zr2O12 doping, J. Alloys Compd., 968 (2023) 10.1016/j.jallcom.2023.171872

[78] J.C. Seol, R. Balasubramaniam, V. Aravindan, R. Thangavel, Y.S. Lee, Ameliorating the electrode/electrolyte interface compatibility in Li-ion solid-state batteries with plasticizer, J. Alloys Compd., 927 (2022) 10.1016/j.jallcom.2022.167077

[79] T. Duan, H. Cheng, Q. Sun, Y. Liu, W. Nie, Y. Chu, Q. Xu, X. Lu, Reinforcing interfacial compatibility of LLZTO/PVDF-HFP composite electrolytes by chemical interaction for solid-state lithium metal batteries, J. Power Sources, 589 (2024) 10.1016/j.jpowsour.2023.233789

[80] X. Liang, Y. Ning, L. Lan, G. Yang, M. Li, S. Tang, J. Huang, Electrochemical Performance of a PVDF-HFP-LiClO4-Li6.4La3.0Zr1.4Ta0.6O12 Composite Solid Electrolyte at Different Temperatures, Nanomaterials, 12 (2022) 10.3390/nano12193390